Phase-field Modeling of Electromigration-induced Defects'

Evolution in Interconnects Films

by

William Farmer

A Dissertation Presented in Partial Fulfillment
of the Requirements for the Degree
Doctor of Philosophy

Approved April 2022 by the
Graduate Supervisory Committee:

Kumar Ankit, Chair
Nikhilesh Chawla
Yang Jiao
Ian McCue

ARIZONA STATE UNIVERSITY

May 2022

ABSTRACT

Electromigration, the net atomic diffusion associated with the momentum transfer from electrons moving through a material, is a major cause of device and component failure in microelectronics. The deleterious effects from electromigration rise with increased current density, a parameter that will only continue to increase as our electronic devices get smaller and more compact. Understanding the dynamic diffusional pathways and mechanisms of these electromigration-induced and propagated defects can further our attempts at mitigating these failure modes. This dissertation provides insight into the relationships between these defects and parameters of electric field strength, grain boundary misorientation, grain size, void size, eigenstrain, varied atomic mobilities, and microstructure. First, an existing phase-field model was modified to investigate the various defect modes associated with electromigration in an equiaxed non-columnar microstructure. Of specific interest was the effect of grain boundary misalignment with respect to current flow and the mechanisms responsible for the changes in defect kinetics. Grain size, magnitude of externally applied electric field, and the utilization of locally distinct atomic mobilities were other parameters investigated. Networks of randomly distributed grains, a common microstructure of interconnects, were simulated in both 2- and 3-dimensions displaying the effects of 3-D capillarity on diffusional dynamics. Also, a numerical model was developed to study the effect of electromigration on void migration and coalescence. Void migration rates were found to be slowed from compressive forces and the nature of the deformation concurrent with migration was examined through the lens of chemical potential. Void migration was also validated with previously reported theoretical explanations. Void coalescence and void budding were investigated and found to be dependent on the magnitude of interfacial energy and electric field strength. A grasp on the mechanistic pathways of electromigration-induced defect evolution is imperative to the development of reliable electronics, especially as electronic devices continue to miniaturize. This dissertation displays a working under-

standing of the mechanistic pathways interconnects can fail due to electromigration, as well as provide direction for future research and understanding.

ACKNOWLEDGMENTS

TABLE OF CONTENTS

LIST OF TABLES

LIST OF FIGURES

xv

Chapter 1

INTRODUCTION

Electromigration (EM) is the transport of material caused due to the momentum transfer between conducting electrons and the diffusing metal atoms ([3]). Technological downscaling has resulted in increased current densities in micro- and nanoelectronic components exposing them to enhanced electromigration which often leads to failure ([4, 3, 5, 6]). Challenges in predicting and controlling the proliferation of EM defects that are borne out of technology scaling has been highlighted in ITRS roadmap of 2011 ([7]). Although electromigration can never be completely mitigated, preventive strategies can help in prolonging the life of electronic circuits. Devising preventive strategies and their efficient implementation warrant a detailed understanding of the failure mechanisms which are directly linked to interconnect microstructure.

EM failure in interconnects manifests in the form of voids and hillocks' formation, grain-boundary slit propagation, surface drift, and metallization; all of which significantly hamper the microelectronics' reliability limiting our capabilities to downscale electronic circuits and chips. Complex interactions of electrical, thermal, and stress fields obscure our understanding of the *diffusion* mechanisms by which EM-mediated failures in interconnects and solder materials occur while making it impossible to predict the onset and propagation of defects. Therefore, a comprehensive understanding of diffusional mechanisms in electronic materials is required for mitigating the deleterious effects of electromigration on interconnect reliability.

In interconnects that comprise of bamboo-like grain structures, GBs are aligned nearly perpendicular to current flow as opposed to a typical polycrystalline microstructure consisting of a random distribution of grains. Bamboo microstructures are more resistant to

1

slit formation due to a 90° misalignment of grain boundaries with respect to current flow. Numerous studies have investigated the defect pathways anticipated in bamboo microstructure, specifically in the context of interconnect reliability ([8, 9, 10]). On the contrary, studies reporting EM-mediated defects in a polycrystalline interconnect consisting of a random distribution of grains have been rare and limited to microstructures comprising of columnar grains ([11, 5, 6]).

Previous finite element studies have shown that interface curvature influences local distribution of electric field ([12, 13, 14]). An increased current density facilitates electromigration more readily, while also increasing Joule heating, locally. Increase in temperature also increases the diffusion rates which accelerates electromigration, while the temperature gradients induced by localized Joule heating can cause thermomigration ([15]). Combined action can result in void and slit formation. Once such defects form, current flows can occur around them diverting the flow of electrons and creating areas of increased current density. An understanding of how these events influence void and slit propagation is important from a fundamental standpoint.

In an inert environment, atomic diffusion along the surface of the interconnect is typically much larger than along the grain boundaries ([16, 17]). However, as interconnects age, they begin to develop surface defects which can not only hamper reliability ([18, 19]) but also enhance the diffusion rates in the grain boundary relative to the surface ([20]). More comparable atomic mobility coefficients along the surface and the grain boundaries can result in distinct defect evolution modes. Moreover, diffusion along grain boundaries and its relative misalignment with the electric current direction can significantly impact the morphological evolution of electromigration-mediated defects. Therefore, the role of grain boundary misalignment and the competing diffusion pathways on the evolution of electromigration mediated defects need to be explored in order to devise techniques for mitigating the interconnect failure. Naturally, this begs the question: how can one pre-

dict the morphological evolution of EM-induced defects in polycrystalline interconnects that may comprise of a network of grain boundaries which are misaligned with respect to the direction of electric current flow? One of the objectives of the present work is to explore this question through the influence of electric current and diffusion pathways on electromigration-induced grain boundary grooving in polycrystalline interconnects. Although isolated attempts for analyzing the evolution of EM-mediated growth of intermetallic compounds (IMCs) [21, 22], slits ([23, 5, 6, 24]), hillocks ([25]), and voids ([26]) have been made in the past via computational or mathematical techniques, the derived models are limited to 2-D and marred with over-simplifying physical assumptions of the physics that govern EM damage. In our recent study, where a 3-D phase-field model to simulate EM-mediated defects has been introduced, the study is limited to columnar polycrystals where the defect pathways are predetermined ([6]). However, predicting the damage pathway is not as trivial in interconnects with non-columnar microstructures which typically comprise of a random distribution of grains. So, previous phase-field studies need to be extended in order to gain a complete understanding of how electric field intensity, grain size, and grain boundary misalignment with respect to applied electric field influence the failure mechanisms.

Building on earlier work ([5, 6]), we begin with isolating the effect of grain boundary misalignment with respect to applied electric field in simulations of slit formation. Then, we simulate the EM-mediated defect evolution in equiaxed polycrystalline microstructure and analyze the mechanisms by which slit formation and surface drift occurs. Next, we examine both these defect evolution modes in a realistic setting comprising of a Voronoi distribution of grains. Also studied is the influence of three-dimensional capillarity on the defect evolution kinetics is explored. The overall goal is to understand the influence of electric field and grain size on the morphological evolution of EM-mediated defects.

Void nucleation can occur from the build up of tensile stresses on the cathode end of

interconnects. This tensile stress accumulation occurs from electromigration driving metal atoms towards the anode. Interconnect failure is largely driven by this process of void nucleation[27, 28, 29]. Void nucleation also occurs at the cathode due to the net diffusion of vacancies opposite the metal atoms, which leads to vacancy accumulation and ultimately void formation. Existing voids can also coalesce during electromigration leading to short circuiting of electronic components and interconnects[30, 31, 32]. From Gan and coworkers, void growth time is directly related to the time-to-failure of copper interconnects [28]. With this, a full understanding of the fundamental mechanisms of void migration and coalescence is needed to best approach failure mitigation in interconnects.

Also studied and presented in this thesis are the dynamics of void migration and growth through coalescence; as these morphological phenomenon are commonly associated with electromigration-mediated failure of interconnects and solders. Many theoretical approaches have been made to investigate migration rates ([33, 2]); however, the utilization of phase-field modeling to study the effects of void migration and coalescence can provide a tool to visualize and quantify the mechanisms of these phenomenon. In this work, we validate our phase field models with previously reported theories of void migration. Also studied is the effect of electromigration on void coalescence rate with accompanied discussion of mechanisms supporting the results. Two phase-field models are utilized here: Model 1, to investigate void dynamics from the perspective of the interconnect; and model 2, an approach to understand the effects of vacancy density. Both models are explained in detail below in Chapter 2. In model 1, we will primarily investigate void migration with anisotropic and isotropic atomic mobilities, as well as void coalescense in 3 dimensions. Model 2 primarily probes the role of eigenstrain on the rates of void migration, coalescence, and budding while simulating from the reference point of vacancy density rather than interconnect density.

Chapter 2 describes the phase field models utilized to simulate electromigration-induced

4

damage in polycrystalline and monocrystalline interconnects. These include the coupled Cahn-Hilliard and Allen-Cahn model which incorporates a non-conserved parameter to distinguish microstructure, and two Cahn Hilliard models without this additional utility.

Chapter 3 provides a comprehensive study of the mechanisms and resulting morphologies of electromigration-induced damage in non-columnar grain systems.

Chapter 4 focuses on the study of electromigration and compressive eigenstrain's effect on void migration, coalescence, and budding in interconnects through the lens of both vacancy and interconnect density simulations.

Chapter 5 concludes the document with the main findings of the work.

Chapter 2

PHASE-FIELD MODELS TO SIMULATE ELECTROMIGRATION MEDIATED
DAMAGE

2.1   Non-columnar Interconnects

Diffuse interface models are driven by the reduction of the total energy of the system.
Here, we present a phase-field model for a periodic array of equiaxed hexagonal grains
representing a polycrystalline interconnect, shown in Fig. 2.4. The region labeled as the
underlayer represents the separation between the interconnect and the dielectric layer. The
phase-field model to simulate EM-mediated defects' growth in interconnects comprising of
equiaxed and random distribution of grains leverages the model already reported in our pre-
vious works except that both those studies were limited to analyzing the damage evolution
in columnar grains[5, 6]. In this context, we would like to clarify that the following model,
whose applicability is limited to the meso length-scale, assumes the interconnect to be free
of any pre-existing point defects of lattice dimension. The conserved order parameter, ρ,
maps the density field such that $\rho = 1.0$ corresponds to the interconnect whereas $\rho = 0.0$
represents the underlayer. The non-conserved parameter, η_i, distinguishes between indi-
vidual grains such that η_i equals 1.0 within the corresponding grain and 0.0 elsewhere. The
density, ρ, is defined such that at the grain boundary there is a small decrease to reflect the
decreased density of a grain boundary. The free energy density functional is given by:

$$F = \int_V \left[f(\rho, \eta_i) + \kappa_\rho \mid \nabla \rho \mid^2 + \sum_i^n \kappa_\eta \mid \nabla \eta_i \mid^2 + f_{em} \right] dV \qquad (2.1)$$

where $f(\rho, \eta_i)$ represents the bulk free energy, the middle two terms dependent on $\nabla \rho$ and
$\nabla \eta_i$ correspond to the diffuse surface and grain boundary energies, respectively, while the

6
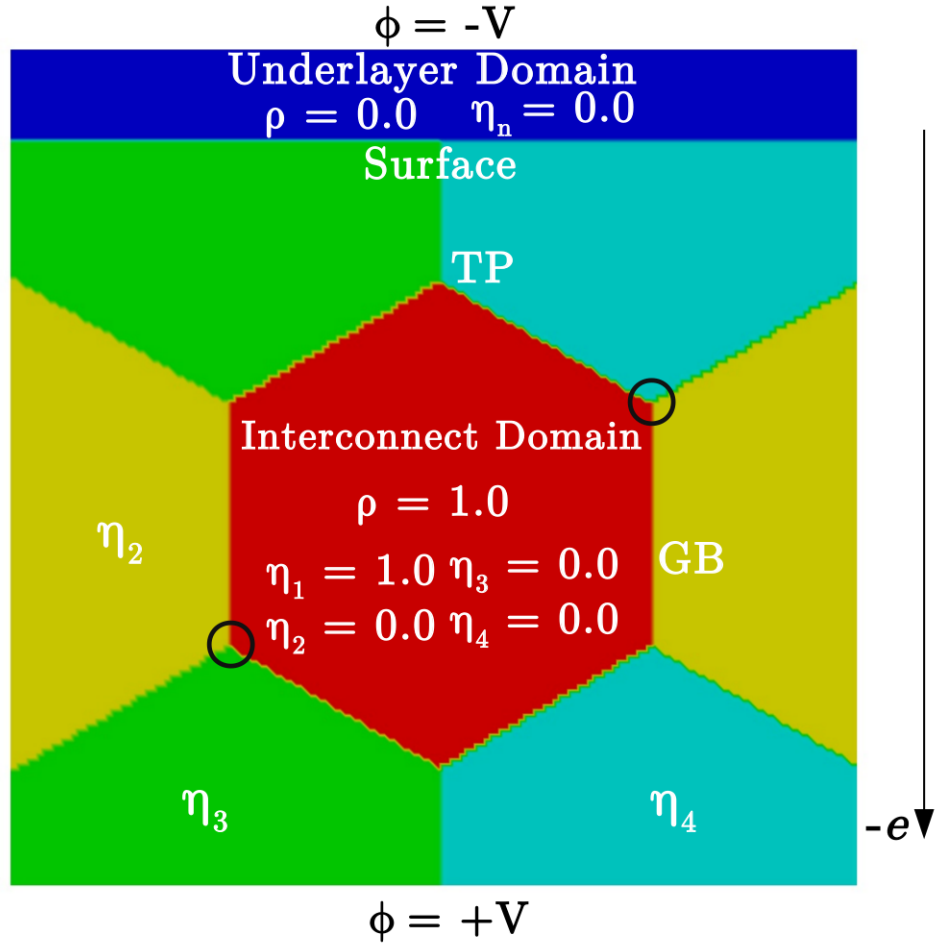
Figure 2.1: Schematic diagram illustrating the initial configuration of the interconnect, which comprises of an equiaxed network of grains, used for phase-field simulations. To distinguish individual grains within the interconnect region, it is sub-divided using the non-conserved order parameter η_i where $i \in \{1, 2, 3, 4\}$). A conserved order parameter, ρ, which represents density, transitions from 0 to 1 across the underlayer/interconnect surface. Grain triple points (TP) and the boundaries (GB) are indicated. Grains size is determined by the distance between circled vertices of hexagonal grains. While no-flux boundary conditions are assigned at the top and the bottom edges of the computation domain, the left and the right boundaries are periodic. Externally-applied electric field is directed normally into the underlayer/interconnect surface.

final term accounts for the electrostatic free energy associated with the externally-applied electric field. κ_ρ and κ_η are the gradient energy coefficients for ρ and η, respectively. The bulk free energy is given by

$$f(\rho, \eta_i) = A\rho^2(1-\rho)^2 + B\rho^2\xi(\eta_i) + C(1-\rho)^2\sum_i^n \eta_i^2, \qquad (2.2)$$

where, A, B, and C are bulk energy coefficients that define the well height in the bulk free energy-order parameter space while $\xi(\eta_i)$ is defined as

$$\xi(\eta_i) = \sum_i^n \left[\frac{\eta^4}{4} - \frac{\eta^2}{2} + 2\sum_{j>i}^n \eta_i^2\eta_j^2 \right] + 0.25. \qquad (2.3)$$

The bulk free energy expression is chosen to ensure free energy minima at $(\rho = 0, \eta_i = 0, \eta_j = 0)$, $(\rho = 1, \eta_i = 1, \eta_j = 0)$, and $(\rho = 1, \eta_i = 0, \eta_j = 1)$ where 'i' and 'j' represent grains in the interconnect. Electrostatic free energy is given by

$$f_{em} = eN_A z\rho\phi, \qquad (2.4)$$

where, e represents the coulombic charge on an electron, N_A is Avogadro's number, z is the effective valence of the species undergoing EM, and ϕ denotes the potential field as defined below in Eq. (2.28). Temporal evolution of density field, ρ, is governed by a Cahn-Hillard equation as a Cahn-Hillard modeled approach [34, 35]:

$$\frac{\partial \rho}{\partial t} = \nabla \cdot M\nabla\mu, \qquad (2.5)$$

where, μ is defined as

$$\mu = \frac{\delta F}{\delta \rho}, \qquad (2.6)$$

such that the temporal evolution is given by,

$$\frac{\partial \rho}{\partial t} = \nabla \cdot M(\rho, \eta_i)\nabla\left[\frac{\partial f(\rho, \eta_i)}{\partial \rho} - 2\kappa_\rho\nabla^2\rho + zeN_A\phi \right]. \qquad (2.7)$$

The atomic mobility, $M(\rho, \eta_i)$ is chosen as

$$M(\rho, \eta_i) = M_b + 4M_{gb}\sum_{j>i}\left[\eta_i^2\eta_j^2\right]^{1/2} + 16M_s\rho^2(1-\rho)^2, \qquad (2.8)$$

8

to account for the variability in atomic mobilities along the surface of the interconnect (M_s), grain boundaries (M_{gb}), as well as in the bulk (M_b). The kinetic equation for the evolution of grain field, η, is described by a system of Allen-Cahn equations [36],

$$\frac{\partial \eta_i}{\partial t} = -L\frac{\delta F}{\delta \eta_i} = -L\left[\frac{\partial f(\rho, \eta_i)}{\partial \eta_i} - 2\kappa_\eta \nabla^2 \eta_i\right], \quad (2.9)$$

where, L is the grain relaxation parameter which determines coarsening rate. The electrostatic field distribution is calculated by solving a Laplace equation

$$\nabla \cdot \left[\sigma(\rho)\nabla\phi\right] = 0, \quad (2.10)$$

where, σ, which represents the electrical conductivity, is linearly interpolated in terms of ρ as

$$\sigma(\rho) = \sigma_{int}\rho + \sigma_{die}(1-\rho), \quad (2.11)$$

with σ_{int} and σ_{die} representing the conductivity of the metallic interconnect and the underlayer region which is composed of a dielectric material, respectively.

Non-dimensionalization of all the above quantities is done by selecting a characteristic energy scale $E' = A'$, timescale $t' = \dfrac{L'^2(\rho'_{int} - \rho'_{die})^2}{M'_b E'}$, and length scale $L' = (\dfrac{\kappa'_\rho}{A'})^{1/2}$.

The coupled system of Cahn-Hillard and Allen-Cahn is solved iteratively using the finite difference method. Grid spacing along both the x and y directions ($\Delta x = \Delta y = 1.0$) is assumed to be equal and the timestep is represented by Δt. A Neumann (no flux) boundary condition is imposed along the y-direction while periodic boundaries, in the x-direction, for effectively allowing a periodic array of interconnects. To investigate the influence of grain size on the morphological evolution of defects, different domains of size $107\Delta x \times 100\Delta x$, $143\Delta x \times 141\Delta x$, $171\Delta x \times 173\Delta x$, and $194\Delta x \times 200\Delta x$ are considered. The equiaxed grain size is defined as the length to join the opposite corners of the hexagon, encircled in Fig. 2.4. For studies involving random grain distributions, the interconnect domain is composed of $171\Delta x \times 173\Delta x$ with $20\Delta x$ assigned to the underlayer domain, which is in contact with the polycrystalline interconnect. This implicitly assigns an average grain size of $102\Delta x$.

9
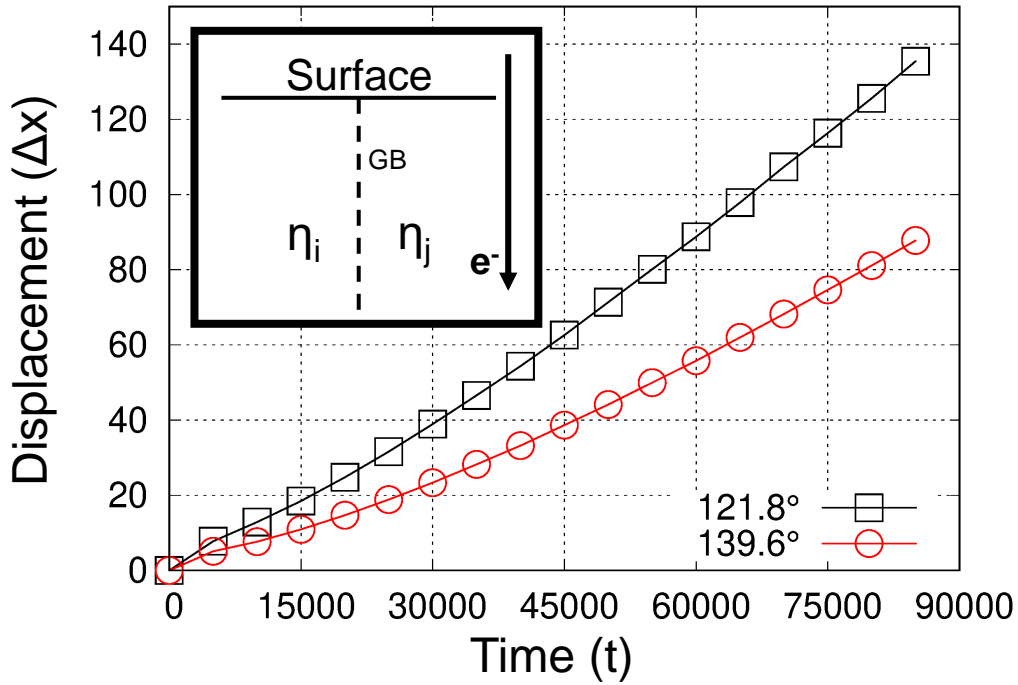
Figure 2.2: A plot depicting the influence the dihedral angle, on the kinetics of slit formation. Both simulations were run with a M_{gb}/M_s of 10^7, $L = 0.1$, and $\Delta\phi = 0.4$. The dihedral angle of 139.6° corresponds to a κ_ρ/κ_η ratio of 3 and is utilized in this present work. A κ_ρ/κ_η ratio of 1 generates a dihedral angle of 121.8°, and the disparate kinetics can be visualized above. The inset represents the initial condition of a bicrystalline interconnect with current flow perpendicular to the surface.

2.1.1 Parameter Selection

Among other external parameters such as the current density, our previous phase-field simulations of EM in columnar grains [5, 6] suggest that the defects' evolution is governed by a ratio of atomic mobilities along the surface and the grain boundaries[5, 6]. Therefore, one method to mitigate defect proliferation is to minimize grain boundaries by increasing grain size. Since interconnects are typically polycrystalline, they offer several pathways for the diffusion to occur. With this prior knowledge, we are able to identify a parameter space

10

of interest an described below.

Table 2.1: Parameters used for simulations reported in Chapter 3. All simulations were run with $\kappa_\eta = 0.33$, $\kappa_\rho = 1.0$, $\sigma_{int} = 3.0$, and $\sigma_{die} = 0.3$.

Simulation	Grain size (Δx)	L	M_b	M_{gb}/M_s	$\Delta\phi$
Influence of GB misalignment	N/A	0.1	10^{-6}	10^7	0.4
Influence of grain size	59, 83, 102, 117	0.1	10^{-6}	10^7	
Influence of electric field	102	0.1	10^{-6}	10^7	0.4, 0.8, 1.2, 1.6 & 2.0
Mixed modes	59	0.1	10^{-6}	$10^3, 10, \& 4$	0.4
Randomly-distributed grains	N/A	0.001 & 0.01	10^{-6}	$10^7, 10^6, \& 10$	0.4

Simulation parameters are selected to isolate different defect modes as well as to inhibit grain coarsening when applicable, as listed in Table 2.1. The three defect modes investigated in this study are slit-formation, surface drift, and mixed modes. Isolated evolution of slits with little to no grain coarsening is necessary to develop a baseline for future studies involving more complex environments such as slit-formation with grain coarsening, anisotropic interface energies, or anisotropic grain boundary atomic mobilities.

2.2 Void Migration and Coalescence

2.2.1 Model 1 - Interconnect Density

Here, we present a model for simulating the evolution of a void in an interconnect. The interconnect material and void are distinguished with the help of scaled density ρ which assumes a value of 1 in the metal region and 0 in the void region. The total free energy

density of the equation is given by

$$F = \int_V \left[f(\rho) + \kappa_\rho |\nabla \rho|^2 + f_{em} \right] dV \tag{2.12}$$

where $f(\rho)$ represents bulk free energy and the second term is the gradient energy term which ensures a smooth variation in ρ. κ_ρ is the gradient energy coefficient. Bulk free energy can be denoted by

$$f(\rho) = A\rho^2 (1 - \rho)^2 \tag{2.13}$$

where A is a constant. The electromagnetic force in equation 2.12 can be expressed as

$$f_{em} = eN_A z \rho \phi \tag{2.14}$$

where e is the electronic charge, N_A is Avogadro's number, z is the valence of species undergoing diffusion and ϕ is the electric potential. The temporal evolution of ρ is given by the well-known Cahn-Hilliard equation [34, 35]

$$\partial \rho / \partial t = \nabla \cdot M \nabla \mu \tag{2.15}$$

where,

$$\mu = \delta F / \delta \rho \tag{2.16}$$

is the chemical potential.

In order to account for difference in mobility in various regions of the system, mobility function is given by the equation

$$M(\rho) = M_b + 16 M_s \rho^2 (1 - \rho)^2 \tag{2.17}$$

where M_b is the bulk mobility and M_s is the mobility at the surface. Since the present work incorporates anisotropic diffusion in metallic crystals, atomic mobility can be expressed as a second-rank tensor such that its magnitude along the x- and the y-axes can be uniquely

defined as M_{xx} and M_{yy}, respectively. Therefore, the mobility tensor, M, is given by

$$\begin{bmatrix} M_{xx} & 0 \\ 0 & M_{yy} \end{bmatrix}. \tag{2.18}$$

In order to couple the physics of electric potential with the phase order parameter, a Laplace equation is used

$$\nabla \cdot [\sigma(\rho)\nabla(\phi)] = 0 \tag{2.19}$$

where σ is the electrical conductivity which is dependent on ρ. By applying a linear interpolation between the metal and void region, we obtain

$$\sigma(\rho) = \sigma_{metal}\rho + \sigma_{void}(1-\rho). \tag{2.20}$$
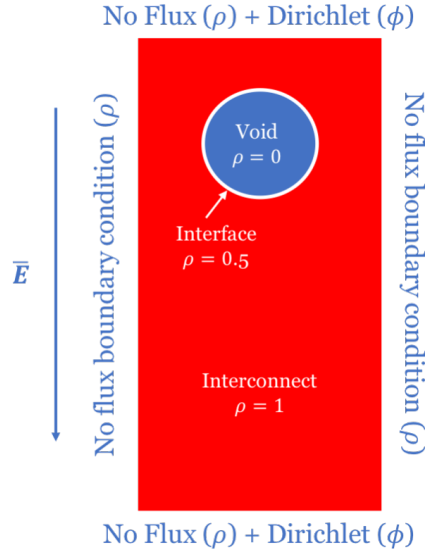
Figure 2.3: A schematic diagram showing the initial condition used for this study.[1]

All the above equations have been non-dimensionalized by considering the energy scale as $E' = A'$, length scale as $L' = (\kappa_\rho'/A')^{1/2}$ and time scale as $t' = L'^2(\rho_{metal}' - \rho_{void}')^2/M_b'E'$. The ratio of conductivity in metal to the conductivity in void, $\sigma_{metal}/\sigma_{void}$ is denoted by

13

β and the potential difference across the length of interconnect is denoted by ΔV. Unless mentioned otherwise, the electric field in our system is aligned along the *y*-axis pointing from top to bottom.

To solve the coupled PDEs, an explicit scheme is employed where the spatial and temporal derivatives are discretized using a central difference and the Euler technique, respectively. The Laplace equation is solved iteratively using a successive-over-relaxation (SOR) method. No-flux boundary conditions are applied for q and ρ at the left and right boundaries. Dirichlet boundary conditions are prescribed for/at the top and bottom edges.

Table 2.2 lists down the parameters that we come across in this model and their respective values which have been used in this study.

Parameter	Value
ρ	0 - 1
β	1-10,000
κ_ρ	1
ΔV	2 - 40
M_s	1 - 2
Δt	0.01
Δx	1

Table 2.2: Simulation parameters used in this study.

2.2.2   Model 2 - Vacancy Density

In this study, we investigate a monocrystalline interconnect, shown in Fig. 2.4. The phase-field model to simulate electromigration in interconnects leverages the model already

14
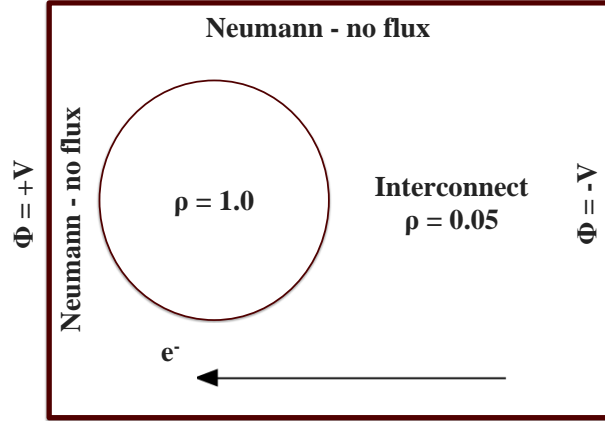
Figure 2.4: Schematic diagram illustrating the initial configuration of the interconnect used for phase-field simulations. Represented above is a monocrystalline interconnect. A conserved order parameter, ρ, which represents vacancy density, transitions from 0 to 1 across the void/interconnect surface. All boundaries are no flux, and the externally-applied electric field is directed down the length of the interconnect.

reported in our previous works except that both those studies were limited to analyzing the defect evolution of slit formation and surface drift ([5, 6]) and modeled the interconnect density rather than vacancy density. Here we expand the model to investigate the migration of voids in 2D due to electromigration by modeling the density of vacancies with $\rho = 1.0$ representing a void in the mesoscale while $\rho = 0.0$ indicates pure interconnect free from vacancies. We utilize a default value of $\rho = 0.05$ in the interconnect to allow for examination of vacancy density evolution throughout our simulations as well as provide an ease to simulation in general, understanding that this far from an equilibrium value for vacancy density. The free energy density functional is given by:

$$F = \int_V \left[f(\rho) + \kappa_\rho \mid \nabla \rho \mid^2 + f_{em} \right] dV \tag{2.21}$$

where $f(\rho)$ represents the bulk free energy, the middle term, dependent on $\nabla \rho$, correspond to the diffuse surface energies, while the final term accounts for the electrostatic free energy

15

associated with the externally-applied electric field. With κ_ρ representing the gradient energy coefficient for ρ. The bulk free energy is given by

$$f(\rho) = \frac{4}{3}\rho^4 - \frac{3}{2}\rho^3 + 0.000001\rho, \tag{2.22}$$

The bulk free energy expression is chosen to ensure free energy minima at $(\rho = 0)$ with ρ representing vacancy density. Electrostatic free energy is given by

$$f_{em} = eN_A z(1-\rho)\phi, \tag{2.23}$$

where, e represents the coulombic charge on an electron, N_A is Avagodro's number, z is the effective valence of the species undergoing EM, and ϕ denotes the potential field as defined below in Eq. (2.28), and $(1-\rho)$ is used to calculate the electrostatic free energy with respect to the interconnect density rather than the density of vacancies. Temporal evolution of density field, ρ, is governed by a Cahn-Hillard equation as a Cahn-Hillard modeled approach [34, 35]:

$$\frac{\partial \rho}{\partial t} = \nabla \cdot M \nabla \mu, \tag{2.24}$$

where, μ is defined as

$$\mu = \frac{\delta F}{\delta \rho}, \tag{2.25}$$

such that the temporal evolution is given by,

$$\frac{\partial \rho}{\partial t} = \nabla \cdot M(\rho, \eta_i) \nabla \left[\frac{\partial f(\rho, \eta_i)}{\partial \rho} - 2\kappa_\rho \nabla^2 \rho + zeN_A \phi \right]. \tag{2.26}$$

The atomic mobility, $M(\rho, \eta_i)$ is chosen as

$$M(\rho) = M_b \rho^3 + 16 M_s \rho^2 (1-\rho)^2, \tag{2.27}$$

to account for the variability in atomic mobilities along the surface of the interconnect (M_s) and in the bulk (M_b). The electrostatic field distribution is calculated by solving a Laplace equation

$$\nabla \cdot \left[\sigma(\rho) \nabla \phi \right] = 0, \tag{2.28}$$

16

where, σ, which represents the electrical conductivity, is linearly interpolated in terms of ρ as

$$\sigma(\rho) = \sigma_{void}\rho + \sigma_{int}(1-\rho).\tag{2.29}$$

2.2.3   Incorporation of Compression on Interconnect

Here, we present a method for the incorporation of an eigenstrain on the interconnect to simulate compression at the anode typically seen in interconnects with cathode edge drift or from packaging methods. We also adopt an elastically inhomogenous model to simulate the 'softness' of a void relative to the interconnect material. These effects can be incorporated via a ρ-dependent elastic energy density term, $E_{el}(\rho)$, which is added to the total free energy density,

$$F = \int_{\Omega} \left[f(\rho) + \frac{1}{2}\kappa|\nabla\rho|^2 + E_{el}(\rho) \right] d\Omega.\tag{2.30}$$

An eigenstrain tensor, ε_{ik}^0, is employed to define the elastic energy density, written as

$$E_{el}(\rho) = \frac{1}{2}\sum_{iklm}(\varepsilon_{ik} - \vec{\varepsilon}_{ik}^0)C_{iklm}(\varepsilon_{lm} - \vec{\varepsilon}_{lm}^0),\tag{2.31}$$

where $\vec{C}_{iklm}$ is the stiffness tensor. The elastic constants of the alloying components are assumed to be distinct, thereby rendering the system elastically inhomogeneous and anisotropic. These are then coupled to the ρ-dependent elastic moduli for the film via an interpolation function, $h(\rho)$ which assumes a value $h(\rho) = \rho^2(3-2\rho)$ [37]. This equation is written as,

$$C_{iklm}(\rho) = C_{iklm}^{\alpha}h(\rho) + C_{iklm}^{\beta}(1-h(\rho)),\tag{2.32}$$

where C_{iklm}^{α} and C_{iklm}^{β} are the elastic constants of the interconnect (α phase) and the void (β phase). The stiffness tensor, C_{iklm} is symmetric under the interchange of i,k for l,m and of i,m for k, l, and has symmetries reflecting those of the crystalline lattice. The

Table 2.3: Elastic constants used to simulate compressed anode end of interconnect

Elastic Constants ($\times 10^{10}$ J/m^3)	A	B
Elastic anisotropy in interconnect - bulk modulus		
C_{11}	48.0	21.0
C_{12}	16.0	16.0
C_{44}	7.0	7.0
Eigenstrain, ε_{ik}	0 to -0.5 %	

eigenstrain is also coupled to ρ by defining the B-rich β phase as the reference phase, such that its eigenstrain vanishes, yielding

$$\vec{\varepsilon}_{ik}^0(\rho) = (1 - h(\rho))\varepsilon_{ik}^0, \tag{2.33}$$

where $\vec{\varepsilon}_{ik}^0$ represents coefficients of the strain tensor which is determined by the crystallography of the phases. The eigenstrain is defined as a fixed parametric value ranging from -5 to 0% to simulate compression in an interconnect.

In a purely elastic framework, mechanical equilibrium is achieved when the cumulative elastic stresses across the film equate to zero, such that

$$\sum_k \frac{\partial \sigma_{ik}(\rho)}{\partial x_k} = 0, \tag{2.34}$$

where the stresses are given by $\sigma_{ik}(\rho) = \partial E_{el}(\rho)/\partial \varepsilon_{ik}$. The system of equations described by equation 2.30-2.34 is equilibriated five times per phase-field time-step. This assumption is justified given that the elastic state of a material, which changes with the speed of sound is faster than atomic diffusion.

To assess the effect of elastic anisotropy during void migration, we define the parameter,

ξ_K, which measures the degree of anisotropy due to bulk modulus, as

$$\xi_K^i = \frac{2\{C_{44}\}^i}{\{C_{11}\}^i - \{C_{12}\}^i}, \tag{2.35}$$

where, C_{11}, C_{12}, and C_{44} are elastic constants and $i \in \{\alpha, \beta\}$, depending on the phase that is being considered. $\xi_K > 1$ signifies that the corresponding phase has a positive elastic anisotropy due to bulk contributions, while a $\xi_K < 1$ signifies a negative contribution.

2.2.4 Numerical Implementation

Non-dimensionalization of all the above quantities is done by selecting a characteristic energy scale $E' = A'$, timescale $t' = \dfrac{L'^2(\rho'_{int} - \rho'_{die})^2}{M'_b E'}$, and length scale $L' = (\dfrac{\kappa'_\rho}{A'})^{1/2}$.

The Cahn-Hillard based model is solved iteratively using the finite difference method. Grid spacing along both the x and y directions ($\Delta x = \Delta y = 1.0$) is assumed to be equal and the timestep is represented by Δt. A Neumann (no flux) boundary condition is imposed along all directions.

Chapter 3

ELECTROMIGRATION-INDUCED DAMAGE IN NON-COLUMNAR

MICROSTRUCTURES

3.1 Non-columnar Microstructures

3.1.1 Influence of GB Alignment on Slit Formation

Starting from a 2-D symmetric grain configuration shown in the inset of Fig. 3.1, we leverage the phase-field model described in Sec. 2.1 to simulate and compare the relative displacements of groove root at distinct GB misalignments ranging from $0°$ to $70°$ with respect to the direction of electric field. One can trivially predict that the groove propagation velocity at finite GB misalignments ($\theta \neq 0$) will scale as $\sec(\theta)$. However, we observe that the average slope $\left(\dfrac{\Delta x}{\Delta t} \right)$ differs by a factor of 3.606 when comparing $0°$ and $60°$ of misalignment with respect to current flow. This outcome demonstrates that the groove velocity scales non-linearly and can be influenced by a number of factors, including grain boundary misalignment with respect to the direction of current flow.

3.1.2 Influence of Grain Size on GB Slit Formation

Here, we investigate the influence of grain size on the morphological evolution of grain boundary slits under EM. Simulated evolution of the slit can be viewed in Fig. 3.2(a-d). With grain boundary atomic diffusivity 7 orders of magnitude above that of the surface and the bulk, the surface drift observed is negligible[6]. Due to the presence of equiaxed grains, the propagation of the slit is symmetrical along the GBs.

The temporal evolution of GB slit, corresponding to a grain size of $102\Delta x$, is displayed in Fig. 3.2(a-d). Slit formation also occurs in simulations with lower grain boundary to

20
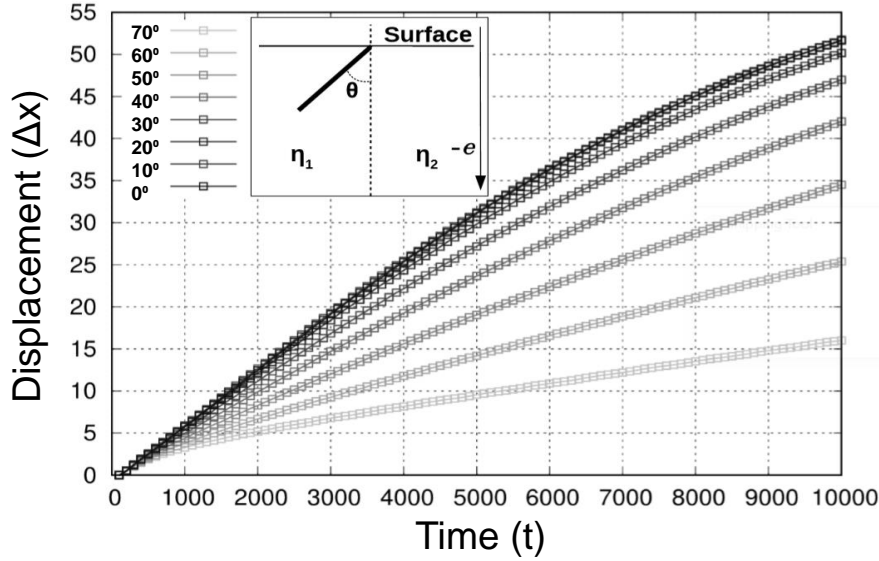
Figure 3.1: A plot comparing the temporal displacement of groove root for distinct misalignments between the grain boundary and the applied current, θ (shown in inset), from $0°$ of misalignment to $70°$. Inset shows the initial configuration wherein surface and grain boundaries are represented by thin- and thick-solid lines, respectively. The dotted line represents the direction along which an external electric current is applied i.e. normal with respect to the interconnect surface.

surface atomic mobility ratios albeit with comparatively slower growth rates. However, surface drift starts to occur at M_{gb}/M_s ratios that are lesser than 100, as discussed in Sec. 3.1.4.

We observe that the average slit formation velocity decreases with an increase in grain size. To characterize the kinetics of slit formation wherein the GB alignment w.r.t. the electric field varies within the polycrystalline interconnect, we plot the temporal evolution of path fraction in Fig. 3.3(a). The path fraction at an instant is calculated as the corresponding length of GB slit, which is measured with respect to the initial position of the interconnect/underlayer surface, divided by the total GB length within the interconnect. The grains here being perfect hexagons, the relative misalignment of the GB can either be
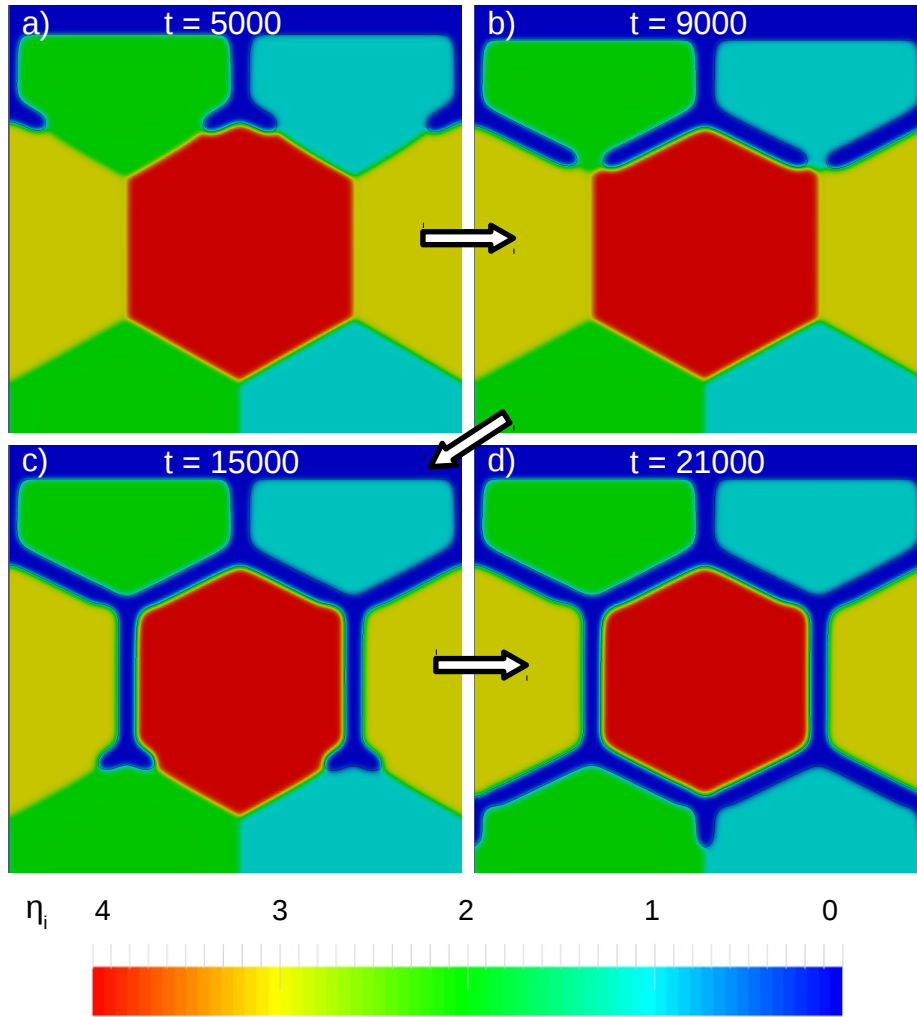
Figure 3.2: Progression of slit formation at intermittent time steps, (a) t = 5000 , (b) t = 9000, (c) t = 15000, and (d) t = 21000. A mobility ratio (M_{gb}/M_s) of 10^7 was used to simulate slit formation. Relaxation parameter, *L*, was set to 0.1 in order to suppress grain coarsening, and a potential difference, $\Delta\phi = 0.4$, is applied such that electric field lines are pointing normally into the interconnect surface. Grain size, as per the definition in Fig. 2.4, is $102\Delta x$.

$0°$ or $60°$ with respect to the direction of the electric field, which results in variable slit growth rates.
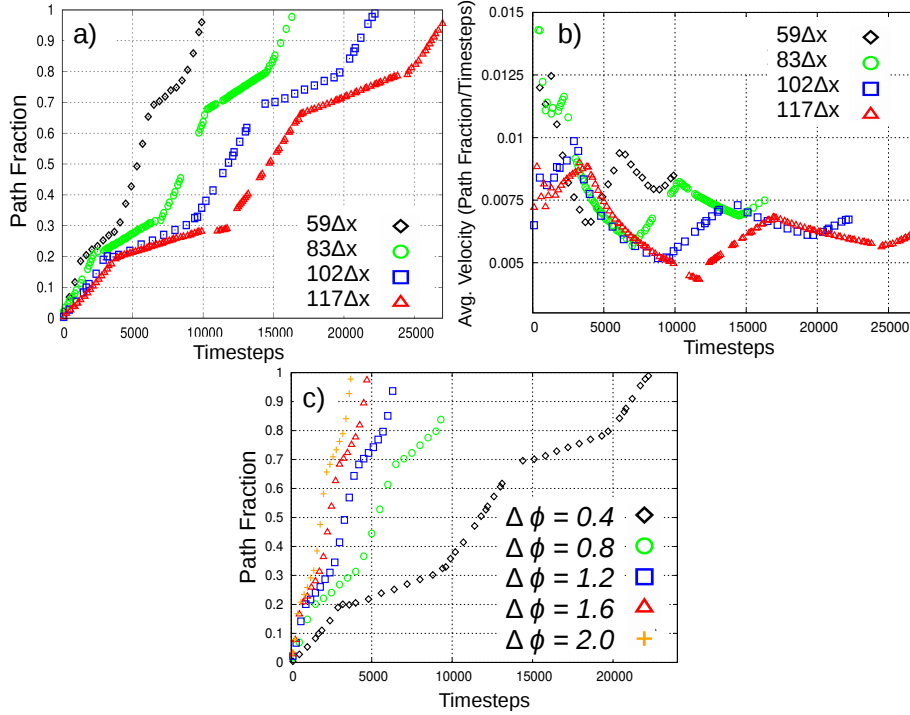
Figure 3.3: (a) Slit path fraction plotted as a function of time highlights the influence of grain size on the velocity of slit propagation. Path Fraction is used to normalize slit length by the maximum displacement of the slit-tip before it touches the bottom edge of the computational domain. (b) Temporal variation in the average velocity of slit tip depicts the influence of grain size on defect kinetics. Simulations reported in (a) and (b) correspond to a mobility ratio (M_{gb}/M_s) of 10^7 which facilitates slit formation, relaxation parameter, L, is set to 0.1 to suppress grain coarsening, and a potential difference, $\Delta\phi = 0.4$, is applied such that electric field lines are pointing normally into the interconnect surface. Grain sizes are chosen as per the definition in Fig. 2.4. The plot in (c) depicts the influence of increasing electric field magnitude on the temporal displacement of the slit tip in a network of equiaxed grains each of size, $102\Delta x$. For the sake of comparison, other materials-specific parameters are kept consistent with respect to (a) and (b).

A decrease in slit propagation velocity in the region of the angled grain boundary is inversely proportional to grain size, as shown in Fig. 3.3(b). The presence of larger grains prolongs failure i.e. the time required for the slit to penetrate completely into the network of grains. However in the context of interconnects, instances when grain boundaries align perfectly with current flow are rare. In Fig. 3.3 (a), the slit propagation rate, represented by the slope, is slightly slower for the first vertical GB when compared to the two sets of vertical grain boundaries following a triple point. Difference between the slopes is attributed to temporally increasing distance between the groove root and the surface exposed to the underlayer region which contributes to a back-fill of the groove roots. As the groove root descends down inside the interconnect, the surface atoms need to progressively diffuse over a larger distance to replenish the groove root. In the first GB section, this distance however is smaller which leads to a reduced growth rate. As the slit descends down, the growth rate increases due to reduction in the back-fill flux which depends on the relative distance between the groove root and surface through the chemical potential gradient dependence.

3.1.3   Influence of Electric Field on GB Slit Formation

In this section, we explore the role of electric field intensity on the kinetics of slit propagation. It is known that current density scales with voltage. In the present model, conductivity, σ, is interpolated in terms of density as shown in Eq. 2.29. Thus, we can investigate the influence of current density by increasing the potential difference, $\Delta\phi$ across the interconnect while keeping the grain size unchanged.

In Fig. 3.4, we visualize the electric field gradient vectors as the slit approaches and traverses past a triple point. The electric field gradient vector is calculated by multiplying the electrostatic free energy density Eq. 2.23 and conductivity at every point on the grid, finding its gradient, and then using vector addition to obtain a net gradient vector.

In Fig. 3.5, we illustrate the temporal changes in the gradient electric field vector, which

24
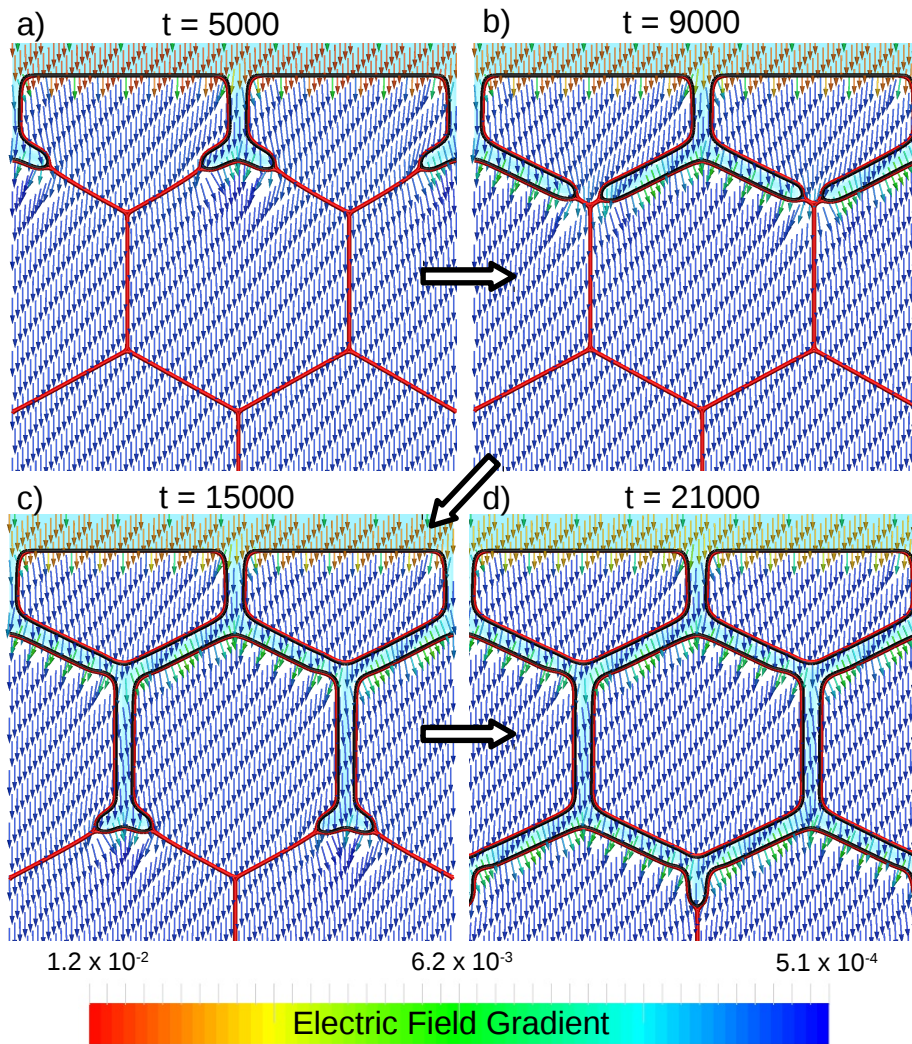
Figure 3.4: Electric field gradient vectors plotted at intermittent timesteps, (a) t = 5000, (b) 9000, (c)15000, and (d) 21000. Sky blue is used to represent the vacuum phase ($\rho = 0$) while the red lines correspond to grain boundaries between the equiaxed grains. For the simulation, following parameters are used: $M_{gb}/M_s = 10^7$, $\Delta\phi = 0.4$, and $L = 0.1$.
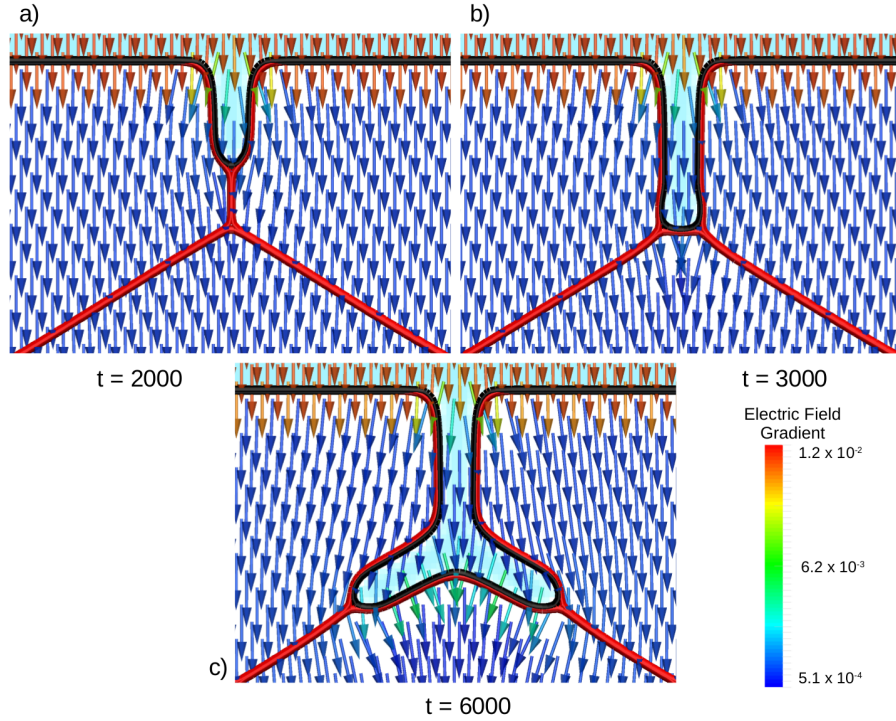
Figure 3.5: Magnified view of electric field gradient vectors displayed in Fig. 3.4 showing behavior of the electric field as the slit approaches the triple point. (a) The slit is approaching the triple point at t = 2000. (b) At t = 3000, the groove root reaches the triple point, and (c) at t = 6000, the slit traverses past the triple point where it splits. Sky blue is used to represent the vacuum phase ($\rho = 0$) while the red lines correspond to grain boundaries between the equiaxed grains.

correspond to Fig. 3.4, plotted at timesteps 2000, 3000, and 6000. The dynamics of slit formation can be visualized in the vicinity of the triple point. Current flow drives the mass along the surface and towards the grain boundary, as seen in Fig. 3.5(a), which facilitates slit formation along the grain boundary. It is worth noting that the subsequent transport of atoms down the grain boundary is largely limited by the value of M_{gb}. In Fig. 3.5(b), it can be observed that the current flow which was initially pushing the atoms along the grain boundary is assisting the transport into the bulk portion of the grains. As the slit

tip progresses, transport into the bulk continues as seen in Fig. 3.5(c). This justifies a decrease in slit formation propagation velocity as plotted in Fig. 3.3(a-c). Comparing the current flow in Fig. 3.5(a) and (c) where the grains are equiaxed, it can be concluded that the wrapping of electric field gradient vectors around the slit influence the growth kinetics. Therefore, in interconnects with non-columnar grain microstructures, a non-homogeneous current flow around the slit tip can cause variable growth rates, which will be discussed further in Sec. 3.2.

In Fig. 3.3(c), we plot the temporal displacement of slit tip at different electric field strengths. It can be observed that the tip velocity increases with the strength of the electric field. Sudden changes in slope can be attributed to misalignment of GB w.r.t. the applied electric field, similar to the plot shown in Fig. 3.3(a).

3.1.4 Mixed Modes

Mixed mode failure caused by electromigration involves slit formation as well as surface drift. Simulations with a M_{gb}/M_s ratio less than 100 depict mixed mode failure as the grain boundary atomic flux is replenished through mass transport from the surface of the interconnect into the groove root. The diffusional mechanism by which such a failure occurs has previously been reported[5] for columnar grains. Here, we analyze the defect propagation rate in a network of non-columnar grains, by varying the ratio, M_{gb}/M_s.

We simulate the morphological evolution corresponding to M_{gb}/M_s ratio of 4, 10, and 1000 to compare the failure rate observed in the three cases, as shown in Fig. 3.6(a), (b), and (c), respectively. As the M_{gb}/M_s ratio decreases, the slit evolution rate becomes more sluggish; however, a relative increase in M_s results in smoother corners along the slit, which intensifies surface diffusion along the slit edges resulting in widening of slits. Surface drift is more prominent in simulations with comparable M_{gb} and M_s. This is due to an occurrence of enhanced surface flux into the groove walls resulting in more mass transport into the

27
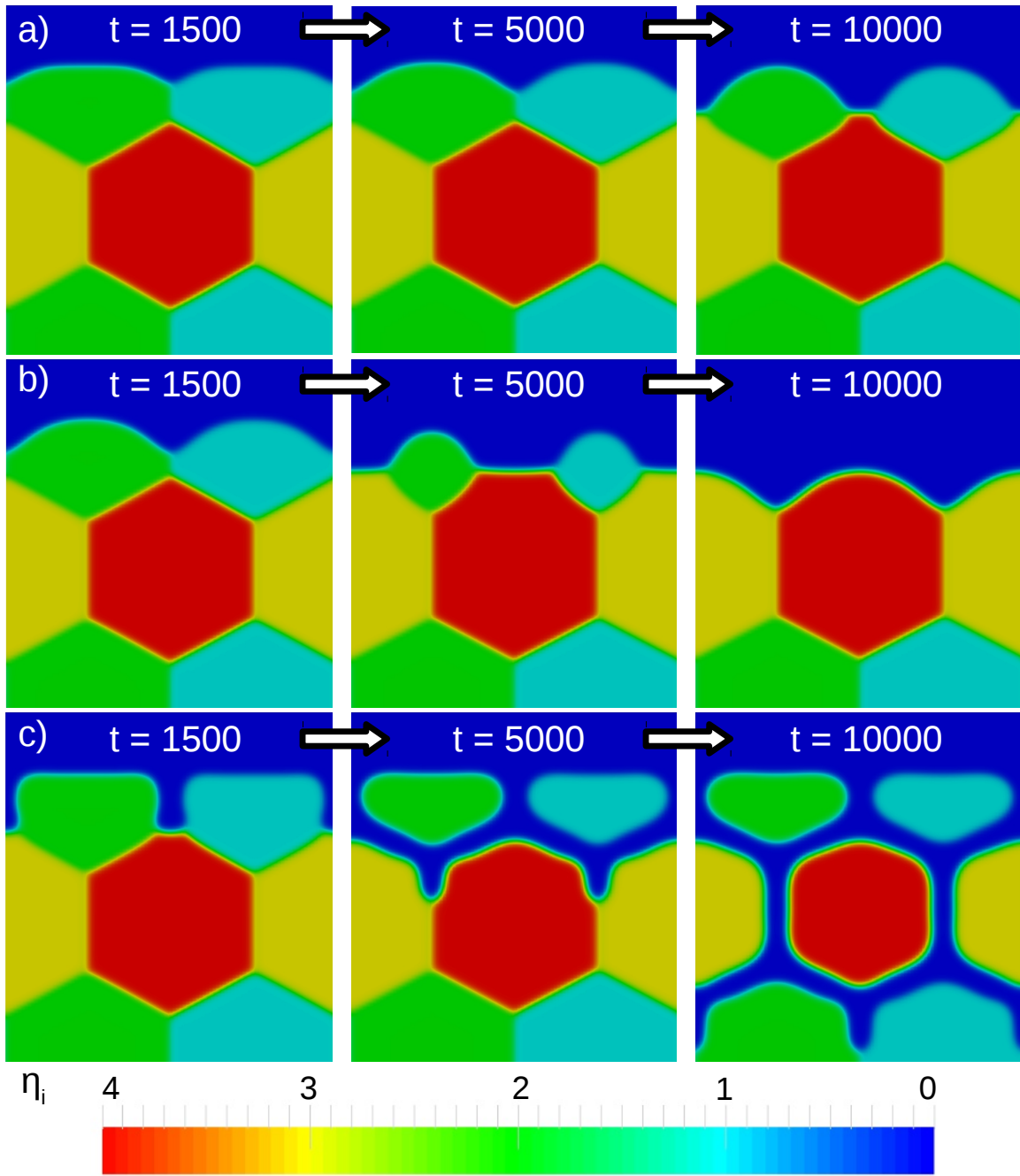
Figure 3.6: Comparison of defect modes at timesteps 1500, 5000 and 10000 for M_{gb}/M_s ratios of (a) 4, (b) 10, and (c) 1000. Parameters, $\Delta\phi = 0.4$, $L = 0.1$, while grain size equals $59\Delta x$.
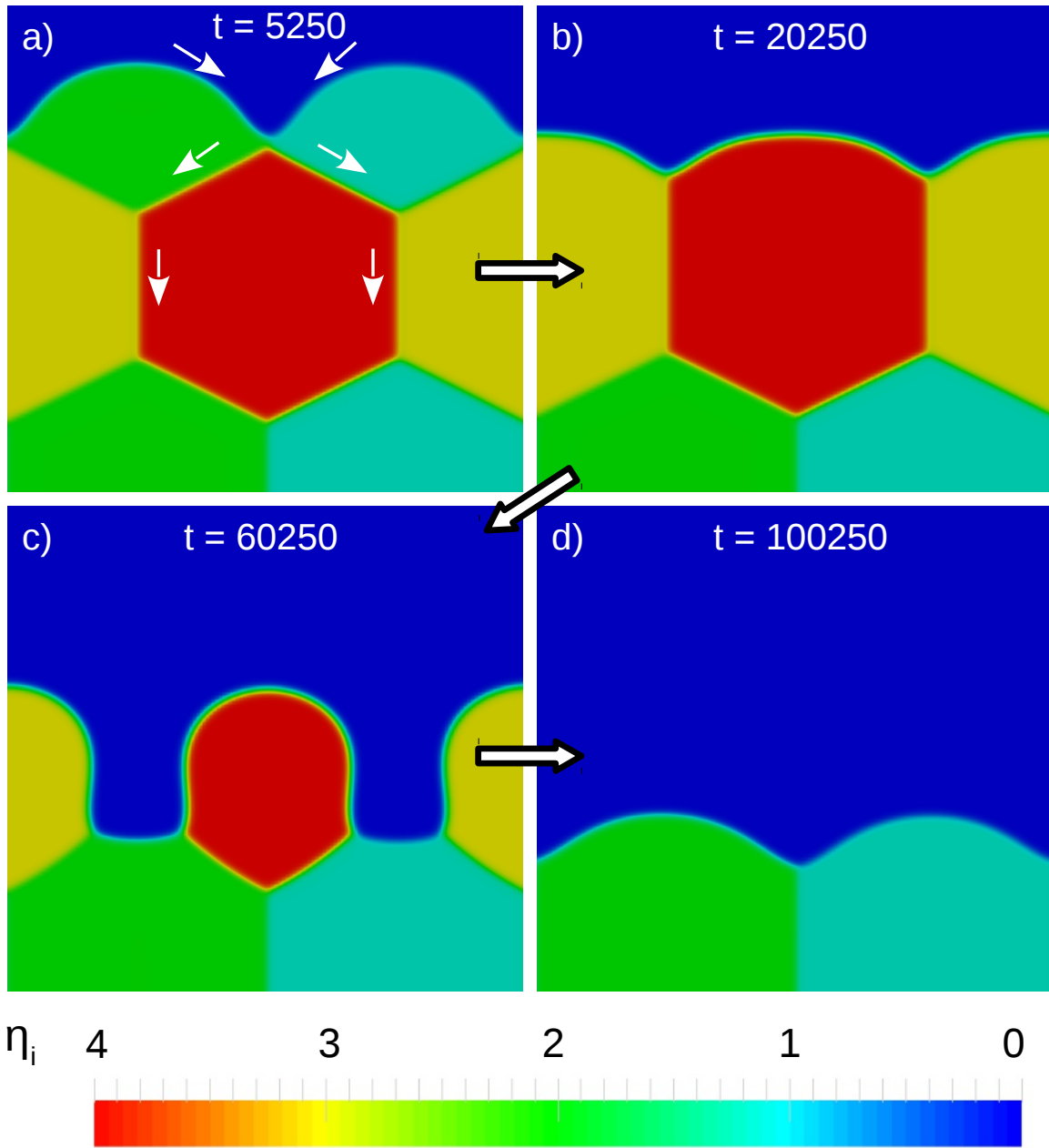
Figure 3.7: Defect propagation at $M_{gb}/M_s = 10$, shown at intermittent timesteps, (a) t= 5250, (b) t = 20250, (c) t = 60250, and (d) t = 100250. Grain size equal $83\Delta x$, assigned as per the definition in Fig. 2.4. For these simulations, $L = 0.1$ and $\Delta\phi = 0.4$.

grain boundary. While diffusion along grain boundaries is not sufficiently high for a slit to form, a lower M_{gb} also results in slower defect propagation.

In Fig. 3.7(a-d), we report the morphological evolution simulated at a M_{gb}/M_s ratio of 10, where a characteristic surface drift, in the direction of applied electric field, is observed. The mechanism by which this phenomena occurs has been reported in our previous work [5, 6]. The phenomenon of surface drift under current stressing was shown to converge towards a global steady state[38] using the level-set method, which is faithfully reproduced in the present simulations, as indicated by the linear portions of the plot in Fig. 3.8(a) that have a non-zero slope. Further, grain size can have a profound influence on the rate of surface drift, as seen in Fig. 3.8(a). From these plots which correspond to different sizes, two distinct steady states are identified. Surface drift occurs at a nearly constant rate until the top two grains are depleted (Fig. 3.7(b)). The direction of diffusion flux that originate at the grain surface and points towards the groove root and subsequently down the grain
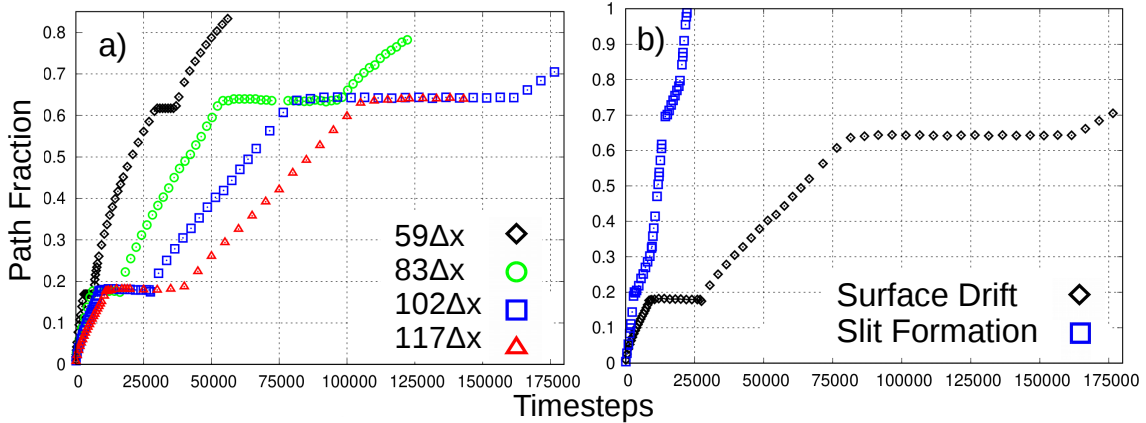
Figure 3.8: (a) Temporal evolution of slit path fraction at M_{gb}/M_s ratio of 10 plotted at different grain sizes. Grain sizes are chosen as per the definition in Fig. 2.4. (b) Temporal evolution of slit path fraction at M_{gb}/M_s ratios of 10^7 and 10 to compare the two defect modes slit formation and surface drift, respectively. Grain size equals $102\Delta x$, $L = 0.1$ and $\Delta \phi = 0.4$.

boundaries is depicted in Fig. 3.7(a). Additionally, the flattened regime in the same plot corresponds to a local steady state of grain consumption following the groove root reaching a triple point. Here, the surface atomic flux, driven by both curvature and electromigration, is positive towards the triple point and GB a diffusional pathway 10 times faster than that of the surface. This results in little to no movement of the groove root at the triple point and consumption of the grains on the surface. The progression of the defect when the number of grains reduces to two (Fig. 3.7(d)) obeys the same kinetics as reported by Mukherjee[5]. Failure caused by surface drift is much slower as compared to slit formation which requires significantly greater mass transport, as depicted in Fig. 3.8(b).

3.2 Randomly-oriented Microstructures

3.2.1 2-D Simulations

In this section, we examine slit formation and surface drift in a more realistic polycrystalline setting which comprises a random distribution of grains. Starting from a Voronoi distribution of grains, we simulate the morphological evolution of defects assuming the same set of simulation parameters described in Sec. 2.1. The relaxation parameter, L, from Eq. 2.9 is assumed to be small ($L = 0.001$) to suppress grain coarsening.

Simulation snapshots plotted at intermittent times in Fig. 3.9 differentiate the morphological evolution at distinct M_{gb}/M_s ratios. The overall failure rate is sluggish at $M_{gb}/M_s = 10$, as opposed to when the ratio is 10^6 times larger due to a transition from surface drift to slit formation regime. The nature of the slit propagation on the right panel is found to be strongly dependent on GB alignment. In Fig. 3.9(b), it is observed that the growth of slits after branching at the triple points, designated by the arrow, along the misaligned GB becomes sluggish or comes to a standstill. On the contrary, slit branches evolving along GBs which are more favorably aligned w.r.t. applied electric field, continue

31
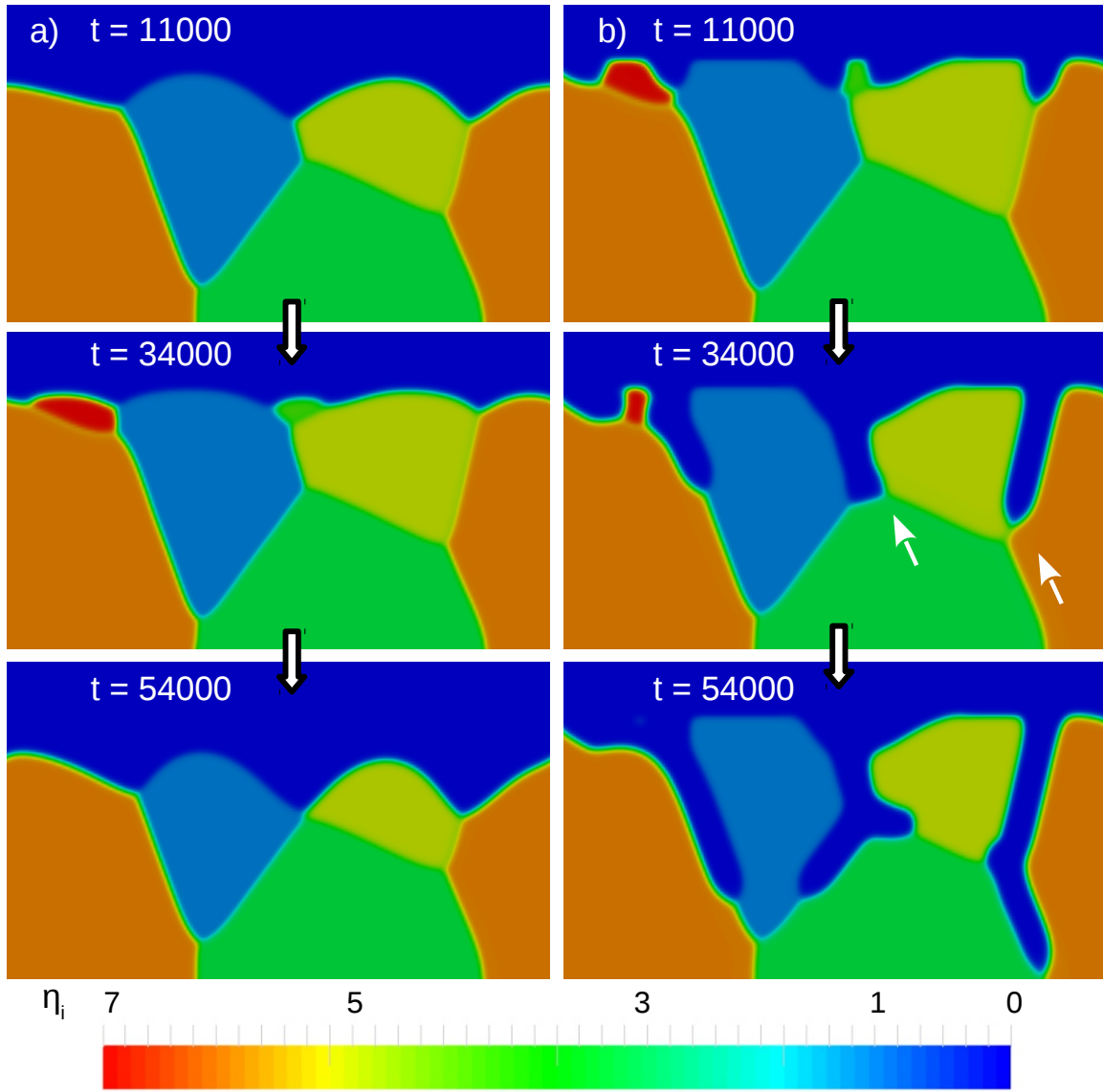
Figure 3.9: Phase-field simulations of (a) surface drift corresponding to $M_{gb}/M_s = 10$ and (b) slit formation corresponding to $M_{gb}/M_s = 10^7$ in an interconnect comprising of a Voronoi distribution of grains. For both the simulations, relaxation parameter, L, is set to 0.001. The potential difference across the interconnect, $\Delta\phi$, is set to 0.4.
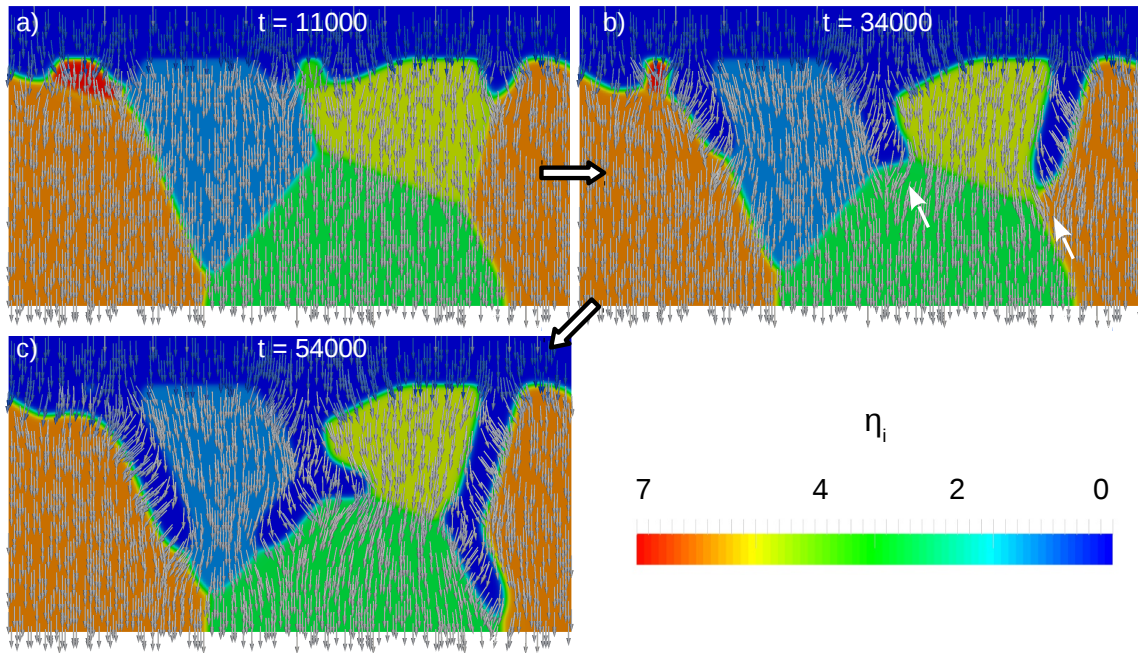
Figure 3.10: Electric field gradient vectors corresponding to the microstructural evolution shown in Fig. 3.9 plotted at intermittent timesteps, (a) t = 11000, (b) t = 34000, and (c) t = 54000.

to progress at the rate determined by relative misalignment, as discussed in Fig. 3.1. In Fig. 3.10, the gradient vector plot composed of arrows allows us to visualize the temporal flow of current around the groove roots as the slits proliferate into the polycrystalline interconnect. Since the GBs of grain designated by η_1 are almost equally aligned w.r.t. current flow, the adjacent groove displacements are nearly equal. On the contrary, slit progression between the GB of η_4 and η_5 is slow. This slowing down of slit progression is characterized by the wrapping of gradient vectors around the slit tip which inhibits the growth. This phenomenom can be further visualized in Fig. 3.11 where we have plotted the density fluxes of an interoconnect with rnadomly oriented grains. The vectors imaged in red represent both direction and scale, which highlights the substantial diffusion around the slits formed. EM-mediated defects' evolution kinetics is thus heavily dependent on grain boundary mis-

alignment with respect to current flow. Therefore, complementary future experiments that can validate the mechanisms proposed through computational studies are desirable.
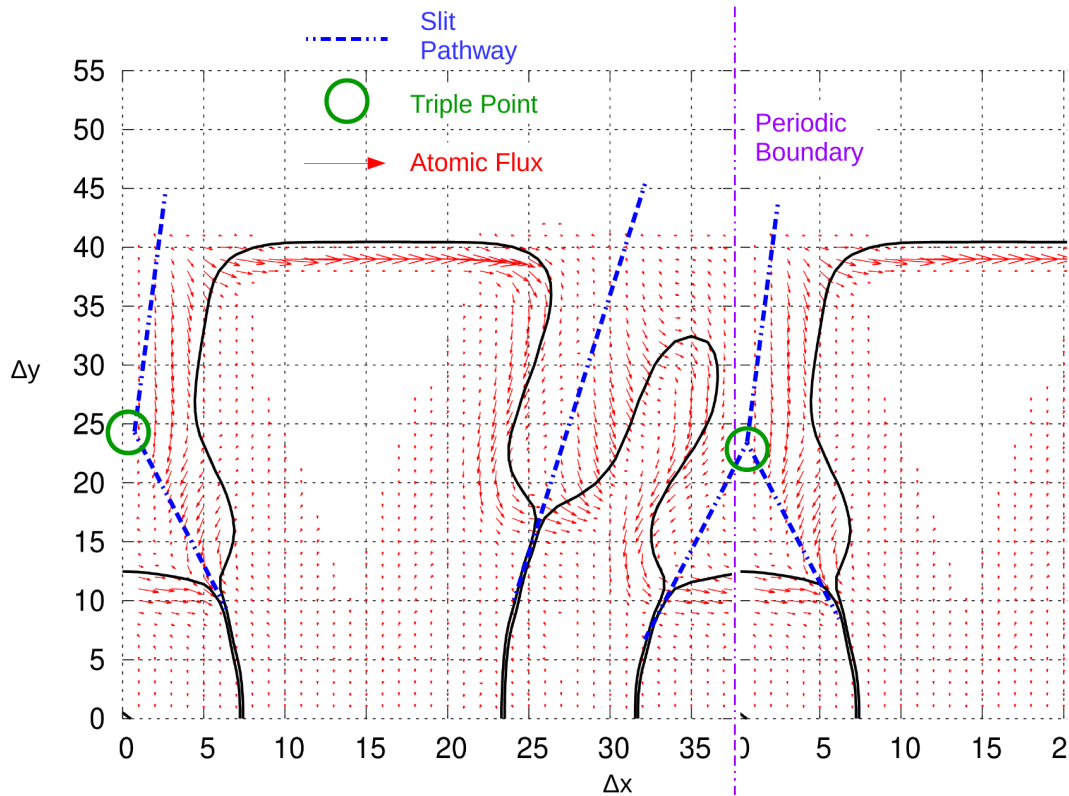
Figure 3.11: 2D flux map for a slit formation simulation with randomly oriented grains. Red arrows represent the direction and cale of density flux with surface and grain contours ($\rho = 0.5$) in black. For all the simulations, $\Delta \phi = 0.4$, $L = 0.001$, and $M_{gb}/M_s = 10^6$.

3.2.2 Influence of 3-D Capillarity

To investigate the influence of three-dimensional capillarity on EM-mediated defects evolution in interconnects comprising of non-columnar grains, we extend our 2-D calculations reported above to 3-D. For this purpose, we generated a random distribution of 3 grains using a Voronoi algorithm in a three-dimensional domain with periodic boundary
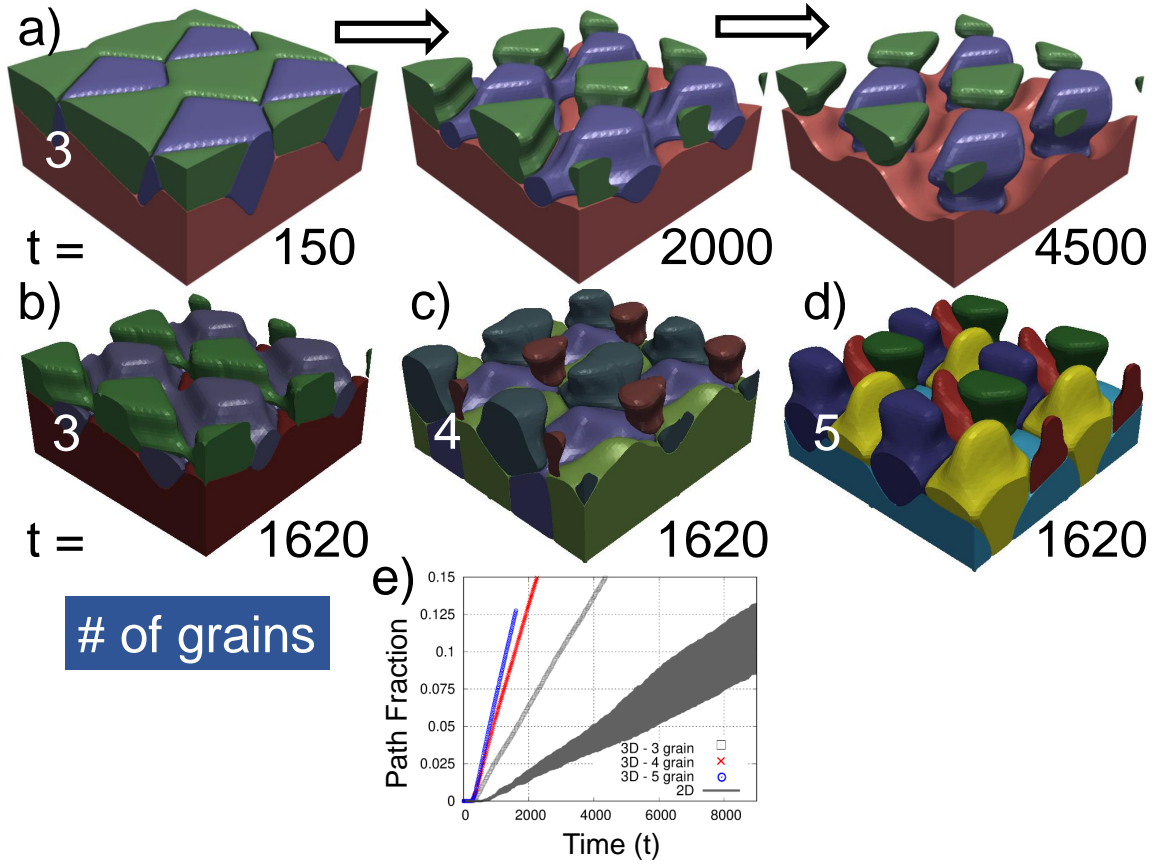
Figure 3.12: 3-D evolution of slits in a network of randomly-distributed grains in (a) at t = 150, 2000, and 4500. To compare grain density effects, we display a 3, 4, and 5 grain interconnect at time 1620 in (b), (c), and (d), respectively. In (e) we compare the temporal slit fraction simulated in 3-D with equivalent 2-D simulations. The 2-D simulations are displayed in the shaded region as the mean $\pm$ the standard deviation in the 2-D displacement plots. The red and blue plots represent the temporal evolution of slit formation in 3-D 4 and 5 randomly-distributed grain interconnects, respectively. This difference in the evolution kinetics highlight the need for 4-D characterization of EM-mediated defects. For all the simulations, $\Delta\phi = 0.4$, $L = 0.01$, and $M_{gb}/M_s = 10^6$.

conditions along the x and y axes and no-flux along the $z-$direction. For comparison with 2-D, several equivalent 2-D domains comprising of distinct distribution of 3 grains are

generated such that the average grain size is retained and is represented by a gray region in Fig. 3.12(e). Preserving the grain size in 2-D and 3-D facilitates a direct comparison of the growth kinetics while mitigating the possibility of grain size effects that can influence defects' evolution (see Sec. 3.1.2). The number of 2-D domains analyzed was kept sufficiently large to minimize statistical errors. Since our aim is to compare the morphological evolution of slits, $\Delta\phi$ is set to 0.4, $L = 0.01$, while the mobility ratio (M_{gb}/M_s) is assumed to be 10^6.

The temporal evolution of slits in a 3-D periodic array of randomly-oriented grains can be seen in Fig. 3.12(a). The shaded region within Fig. 3.12(e) is the mean slit evolution rate for the 2-D simulations which accounts for the standard deviation. While the slit evolution rates in 3-D as well as 2-D, on an average, follow a linear trend, the slope of the former is found to approximately three times larger than the latter when considering grains of similar sizes. This can be attributed to a multitude of diffusional pathways that are available in 3-D as opposed to 2-D where the evolution is constrained along a line. The plot in Fig. 3.12(e) shows that the 3-D failure rate increases with an increase in GB density or with grain refinement with a direct comparison displayed in Fig. 3.12(b-d). As the number of grains are increased without altering the size of 3-D computational domain, the discrepancies in predicted failure rates is found to decrease which indicates the importance of large scale studies. Finally, while an accurate prediction of defects' evolution rate warrants large scale studies comprising of thousands of randomly-oriented grains, in all certainties, our findings highlight the pressing need for future characterization studies in 4-D.

Chapter 4

EFFECTS OF ELECTROMIGRATION ON VOID MIGRATION AND COALESCENCE

4.1   Model 1 - Interconnect Density

4.1.1   Validation of Model 1

To begin we validate our phase-field model with theoretical and standard relationships when studying void migration in interconnects. Below in Fig. 4.1, we plot our simulations at three different atomic mobilities and $\Delta\phi's$, and fit the data to the following relationship [33]:

$$ln(\frac{vT}{j}) = ln(\frac{D_oZ^*e\rho}{k}) - \frac{Q}{kT}, \tag{4.1}$$

where v is void velocity, T is temperature, j is current, D_o is the diffusion coefficient of the interconnect, Z^* is the effective charge, e is electron charge, ρ is the resitivity of the interconnect, k is Boltzmann's constant, and Q is the activation energy to move an atom in the interconnect. Atomic mobility is directly related to temperature, so to simulate void migration at different temperatures, atomic mobility is varied in its stead. Similarly, current is related to potential difference by Ohm's law; therefore, if conductivity is held constant, a change in $\Delta\phi$ is linearly related to a change in current, j. Our simulations use the following parameters: $\Delta\phi = 0.5, 2.0$, and 4.0 and $M_b = 0.5, 1.0$, and 1.5. Fig. 4.1 demonstrates the predicted behavior of void velocity's dependence on current and temperature, validating the phase field model.

Further, we compare results from phase field simulations to the work of Artz et. al. [2]. They propose the behavior of void velocity will decrease with an increase void radius
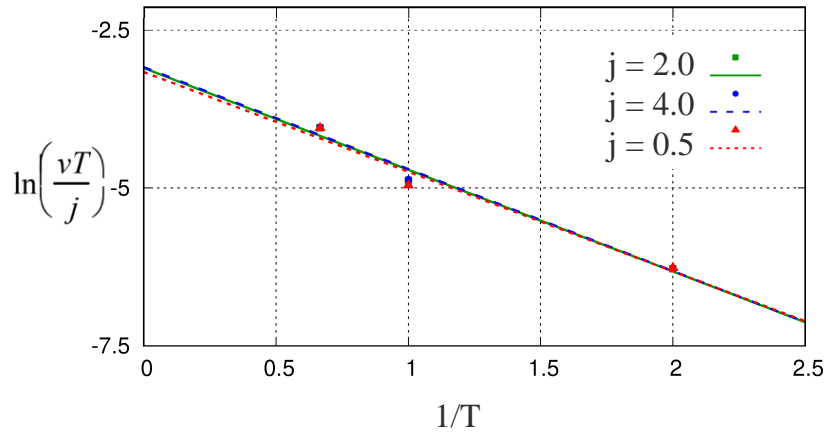
Figure 4.1: Plotted above is the void migration velocities for 3 different $\Delta\phi$ (0.5, 2.0, and 4.0) by the reciprocal of temperature. The $\Delta\phi$ parameter stands in for current density, j, as they are linearly related via the conductivity of the material which remains constant between these simulations. Temperature, here, is represented in the model by three different atomic mobilities, and the data is fit 4.1. Simulation parameters: $\Delta\phi = 0.5, 2.0$, and $4.0, M_b = 0.5, 1.0$, and 1.5.

until the size of the void is large enough to confine the void within the interconnect, which increases the current density around the void and therefore elctromigration. Ignoring confinement of the void in the interconnect, our simulations were used to fit the first part of this model as depicted in Fig. 4.2. On the left of this figure, we have included some of Artz's work for comparison with the right hand side of the figure where plotted is the relationship between void radius and velocity. The general trend from the cited work and our simulations is $1/r$. As our work was performed in a parametric space and the variables in the equation except radius and velocity are constant, all that is needed is replication of this

38

general trend to further validate our model.
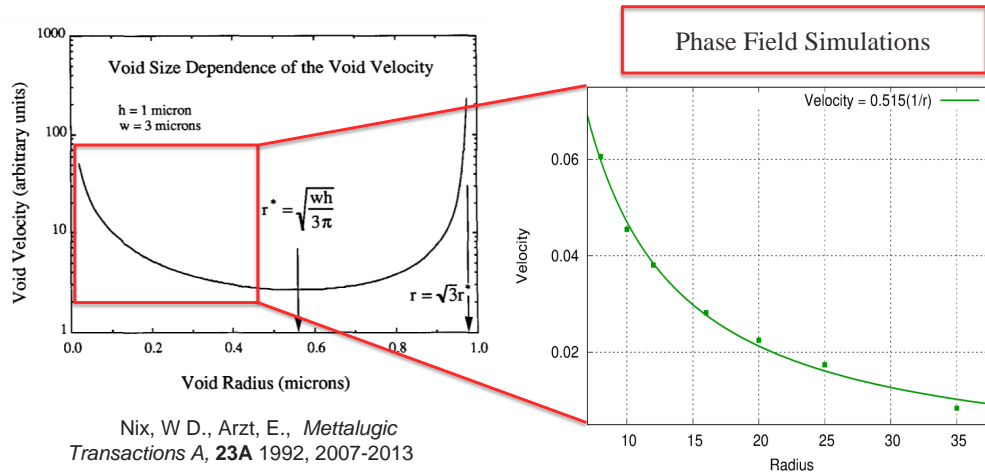
Figure 4.2: Plotted on the left is a figure from Artz and coworkers [2] representing the relationship of void velocity and void radius. On the right, we have plotted the phase field data for void migration velocity by void radius fit to the theory presented in their work. Simulation parameters: $\Delta\phi = 4.0, M_s = 1.5$, and $M_b = 10^{-6}$.

4.1.2 Isotropic Atomic Mobility

In this following study, atomic mobility is assumed to be isotropic to investigate the effects on void migration from the parameters of potential difference, $\Delta\phi$, and atomic mobility of the void surface, M_s. This work was done in conjunction with Shivani Vemulapalli during her masters thesis [1] and will be summarized here for completeness. As visible in Fig. 4.3, the leading edge of the void elongates and migrates significantly quicker with

increased potential difference. We observe this phenomenon due to the increased electro-migration associated with the increased potential difference, and this result is replicated in model 2, the vacancy diffusion formulation, in the images of void budding in Fig. 4.18 and 4.19 discussed in Sec. 4.2.2.
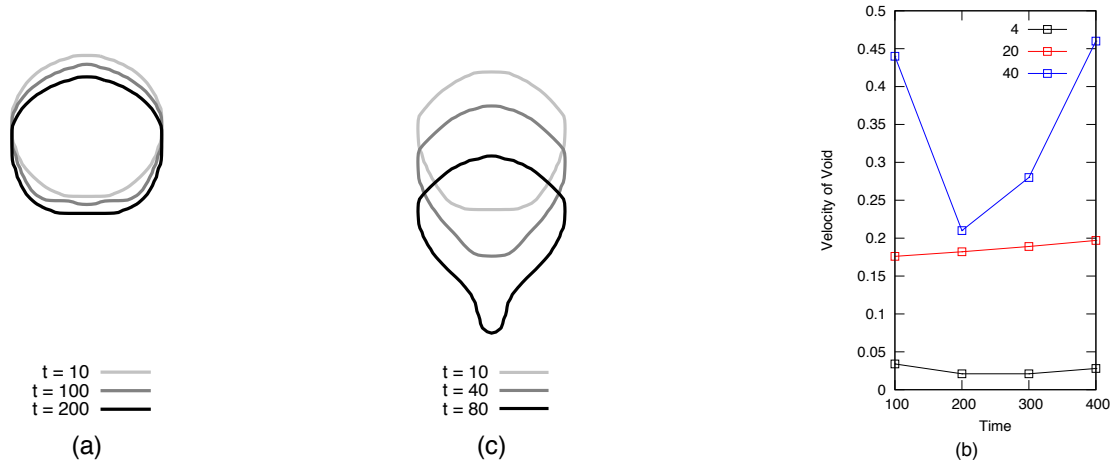
Figure 4.3: Images above are the morphological differences of void evolution for two potentials, $\Delta\phi$. Contours of $\rho = 0.5$ are plotted for simulations of ΔV of (a) 4, (b) 40 with a comparison velocities in (c).[1]

Stronger potential differences impart more momentum to electrons passing through the interconnect increasing electromigration, especially of atoms along the surface of the void. However, the surface of the void is partially governed by capillary forces attempting to reduce additional curvature and energy of the system. As these competing forces inter-act, electromigration driving the elongation of the void and capillary forces maintaining the circular nature, void morphology is effected and capillarity is overpowered at higher electric potentials. This phenomenon is further explored with a study increasing the atomic mobility along the surface of the void.

As atomic mobility increases at the void surface, elongation of the leading void edge is observed as well as quicker void migration rates as seen in Fig. 4.4. This is due to

a similar force balance as described above; however, increasing atomic mobility of the surface increases the rate at which capillary action can resolve the unfavorable energetics of elongation caused by electromigration. This results in a more compact and less extreme elongation of the void displayed in Fig. 4.3.
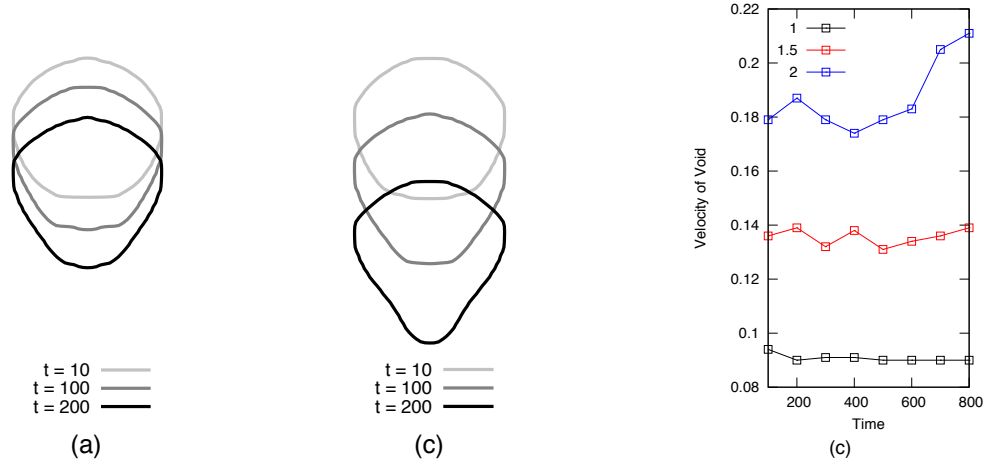
Figure 4.4: Comparison of void morphologies with different surface atomic mobilities. Contours of $\rho = 0.5$ are plotted for simulations with surface atomic mobilities, M_s, of (a) 1 and (b) 2. Plotted in (c) is a comparison of void velocities with different values of M_s. [1]

4.1.3 Anisotropic Atomic Mobility

Also in conjuction with Shivani Vemulapalli, we study the effects of an anisotropic atomic mobility with increasing electric potential on migrating voids due to electromigration.[1] Using Eq. 2.18, we assign a 10x larger atomic mobility in the x direction of the simulation. From these simulations we observe a widening of the void's trailing edge when there is substantial void migration, which is followed by a newly observed morphology, the swimming void morphology. The widening of the void is due to the increased lateral mass transport with larger atomic mobilities in the x-direction; however, the swimming void morphology, which is characterized by a elongation and contraction of the lateral edges of the void, is

formed due to a cycle of void elongation from the increased mass transport in the x direction, over-extension of the void to a sharp corner, and then contraction of this sharp edge due to capillary forces minimizing curvature of the void's lateral edge. Increasing electric potential exacerbates this destabilization of the void edge, and Fig. 4.5 demonstrates the void morphologies with Fig. 4.6 (a) displays the oscillating nature of the void edge at larger potentials.

t = 10	t = 10	t = 10
t = 100	t = 100	t = 100
t = 200	t = 200	t = 200
(a)	(b)	(c)
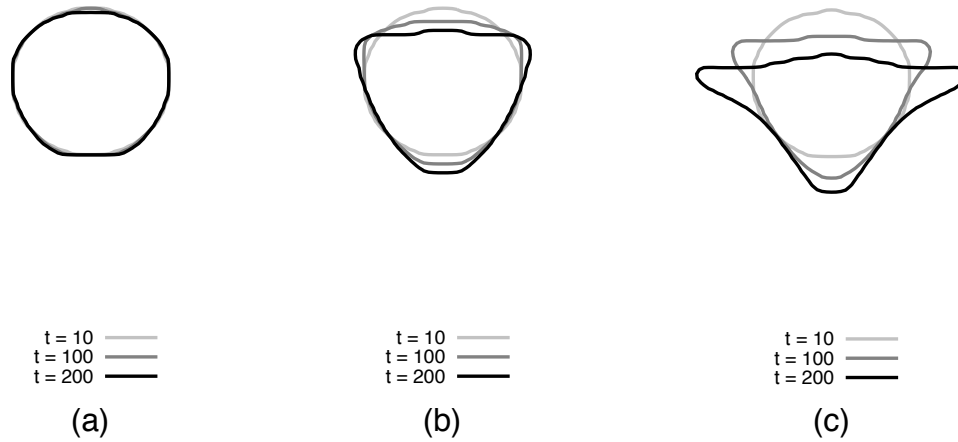
Figure 4.5: Influence of potential difference magnitudes on the morphological evolution of void. Contours of $\rho = 0.5$ display the temporal evolution of void morphologies simulated when $\Delta\phi$ equals (a) 2, (b) 10 and (c) 20. [1]

4.1.4   Bicrystalline Interconnect

Here, we coupled model 1 with an Allen-Cahn formulation like described in Sec. 2.1 to investigate the dynamics of void migration in two bicrystalline environments: one with a grain boundary perpendicular to current flow and one parallel. The simulations depicted below had a domain size of $300x100\Delta x$, $\kappa_\eta = 0.33, \kappa_\rho = 1.0, \Delta\phi = 2.5, M_s = 1.5, M_{gb} = 10^{-5}$, and $M_b = 10^{-6}$. M_s was made much larger to represent the quicker diffusion along the void's surface, while M_b and M_{gb} were made equal to focus the study on the void behavior.
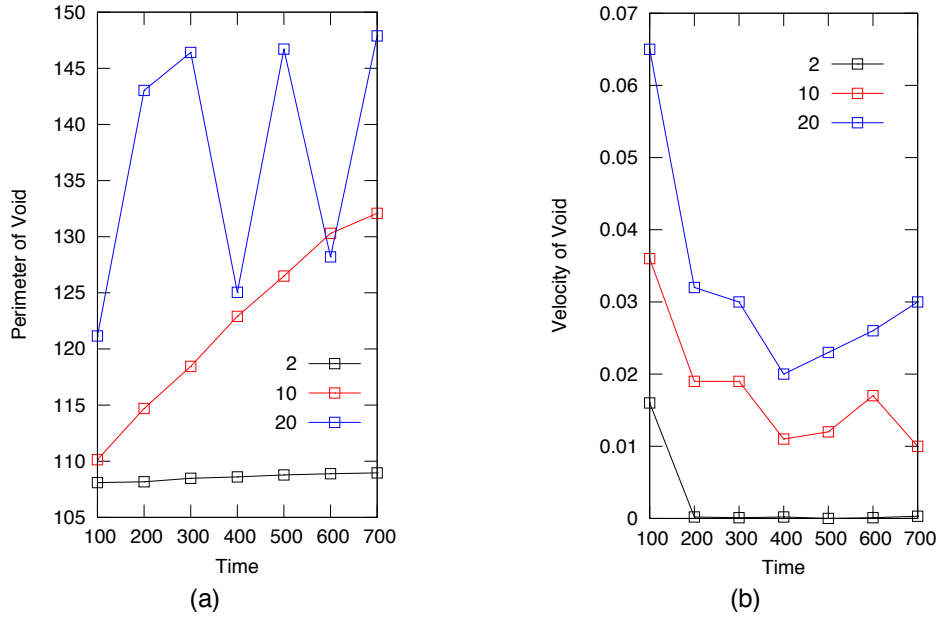
Figure 4.6: Analyzing the influence of potential difference, $\Delta\phi$, on the simulated void kinetics. Plots show the temporal evolution of void (a) perimeter and (b) velocity for distinct values of ΔV ranging between 2 and 20. [1]

Void migration along a grain boundary parallel to current flow is represented in Fig. 4.7 at times steps of 50 (a), 500 (b), and 700 (c). Here we can visulize slight void elongation along the grain boundary as well as rather unimpeded void migration. Void elongation occurs due to the increased atomic mobility along the surface of the void relative to the grain boundary and bulk of the interconnect. In simulations of void migration with a grain boundary perpendicular to current flow, as visualized in Fig. 4.8, elongation is not observed. In (b) of Fig. 4.8, the grain boundary deforms to meet the migrating void due to the decreased energy penalty of reducing the surface area of the grain boundary as some of it combines with the void surface. Throughout this process, the void remains solidly circular. As the void continues to migrate and begins to pin the grain boundary, the grain boundary is further deformed. This process slows the void's migration rate.
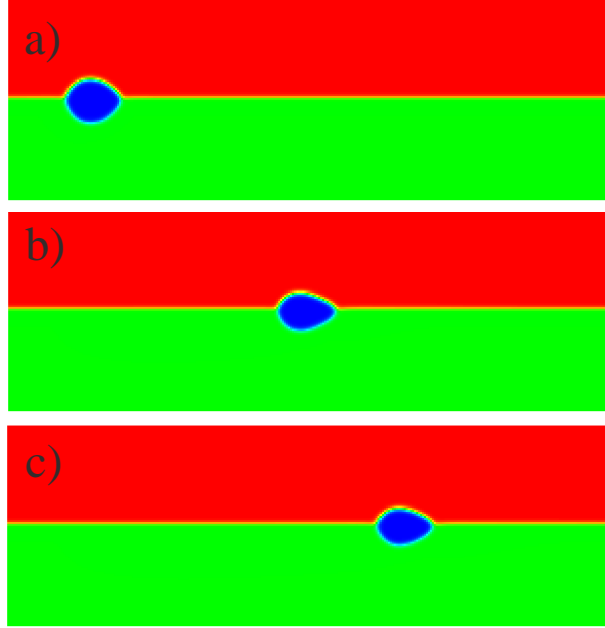
Figure 4.7: Imaged here is the void migration at times of 50 (a), 500 (b), and 700 (c) along a grain boundary parallel to current flow from a simulation with parameters $\Delta\phi = 2.5, M_s = 1.5, M_{gb} = 10^{-5}, and M_b = 10^{-6}$ Green and red represent the separate grains and the blue region is a void where $\rho = \eta_i = 0.0$

4.1.5   3-D Comparisons and Void Coalescence

3-D simulations of void coalescence and budding were performed to analyze the effects of 3-D capillarity. In Fig. 4.9, we display the 3-D evolution of void coalescence of a void pair with radii of 15 and 25 at times of 100 (a), 2000 (b), and 4000 (c). Colored in the image are the z-normals to help instruct the 3-D nature of the void. The smaller trailing void migrates quicker, as previously discussed, and merges with the larger leading void depicted in Fig. 4.9 (b). This process continues into (c) with nearly full resolution of the void pair. Plotted in Fig. 4.10 are comparisons of void coalescence in 2- and 3-dimensions as well as with and without electromigration. These simulations were of coalescing void pairs with radii of 15 Δx and $\Delta\phi = 0.0, 8.0$. From this figure, we can draw multiple conclusions.
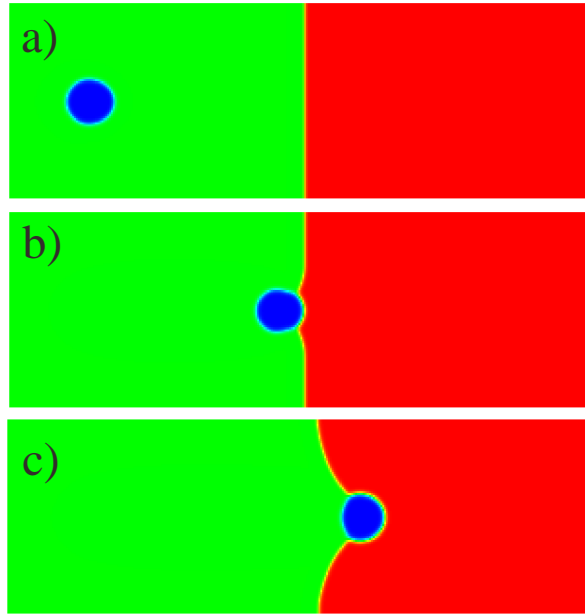
Figure 4.8: Imaged here is the void migration at times of 50 (a), 500 (b), and 700 (c) along a grain boundary perpendicular to current flow from a simulation with parameters $\Delta\phi = 2.5, M_s = 1.5, M_{gb} = 10^{-5}$, and $M_b = 10^{-6}$ Green and red represent the separate grains and the blue region is a void where $\rho = \eta_i = 0.0$

First we can see that early coalescence is identical across all deminsionality and electromigration strength; however, the void pair coalescing with electromigration remains more tubular than spherical, resulting in a smaller overall neck length. This can be attributed to electromigration being strong along the sides of the void pair during coalescence, as there is a period where the length of the void pair along the direction of current is larger. Further tests of void pairs coalescing perpendicular to current would be needed to test this. Secondly, the effects of electromigration are magnified in 3-D when compared with 2-D. This can be seen from the differences in neck length for simulations with electromigration relative to the nearly identical curves for simulations without electromigration. The additional dimension of electromigration overpowers the additional dimension of capillarity resulting

in a smaller neck length and more tubular equilibrium shape.
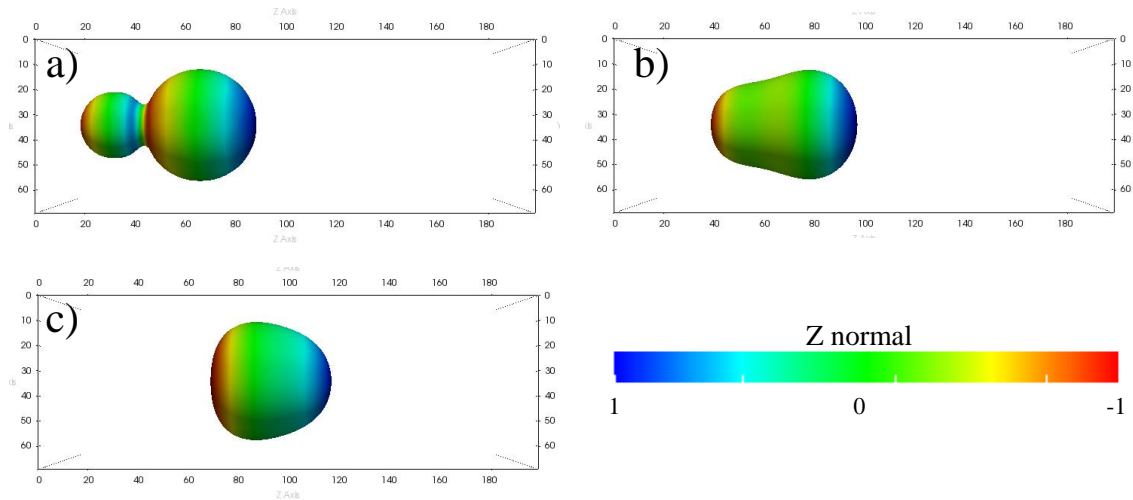
Figure 4.9: Above is a simulation of void coalescence at times of 100 (a), 2000 (b), and 4000 (c) with a trailing void of radius 15 and leading void with a radius of 25 Δx. Simulations used the following parameters: $\Delta\phi = 8.0, M_s = 1.5, M_{gb} = 10^{-5}$, and $M_b = 10^{-6}$. Color scheme is of z normal values along the contour of $\rho = 0.5$ to help indicate the 3D structure in the image.

Finally we visulize the budding behavior of a void pair in 3-D as displayed in Fig. 4.11 at times of 100 (a), 2000 (b), and 4000 (c). Here, we use the same simulation as in Fig. 4.9 with the trailing and leading void sizes swapped to demonstrate the budding behavior of a smaller void from a larger void. As the leading void migrates away from the center of the void pair, elongation of the necking region is seen. This neck continues to decrease in size as the smaller void moves away until budding occurs. This behavior is similar to what we see in the Sec. 4.2.2 and will be explained in more detail there.
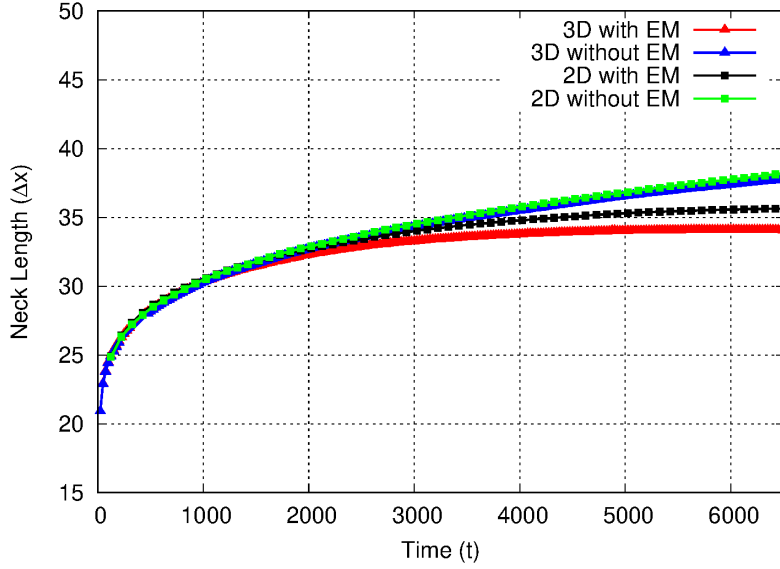
Figure 4.10: Plotted here are comparisons of 2- and 3-D neck lengths of coalescing void pairs with radii of 15 Δx with and without electromigration ($\Delta \phi = 0.0, 8.0$). Simulations used the following parameters: $\Delta \phi = 0.0 \text{ and } 8.0, M_s = 1.5, M_{gb} = 10^{-5}, \text{ and } M_b = 10^{-6}$.

4.2   Model 2 - Vacancy Density

Next, we expand the model demonstrated in Sec. 4.1 to simulate the diffusion of vacancy density rather than interconnect density. This method provides the same dynamics that were explored in model 1 and allows us to examine the diffusion of vacancy density within an interconnect as well. Comparisons to results in this section and Sec. 4.1 will be explored were applicable to demonstrate the congruence between the models and serve as validation for the model 2. Equilibrium vacancy density is dependent on a variety of parameters, and these values are outside the range of feasibility in phase field modeling. Therefore we have chosen a value of 0.05 to represent the initial vacancy density in the interconnect. We find this relatively large value acceptable as we are not interested in the nucleation of microvoids or substantial volume additions to the voids simulated, but more
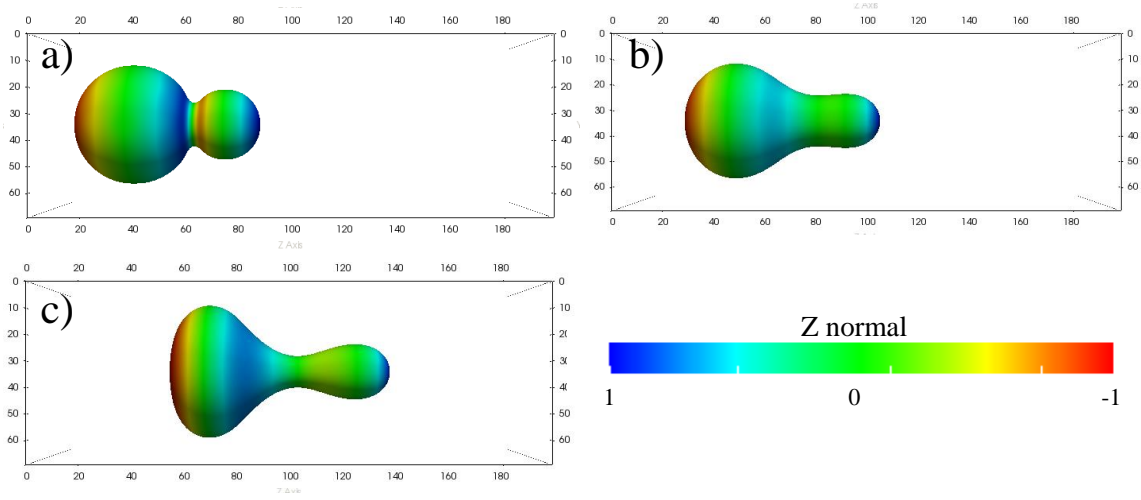
Figure 4.11: Displayed above is a simulation of void budding at times of 100 (a), 2000 (b), and 4000 (c) with a trailing void of radius 25 and leading void with a radius of 15 Δx. Simulations used the following parameters: $\Delta\phi = 8.0, M_s = 1.5, M_{gb} = 10^{-5}$, and $M_b = 10^{-6}$. Color scheme is of z normal values along the contour of $\rho = 0.5$ to help indicate the 3D structure in the image.

the behavior of vacancy density in the environments simulated.

4.2.1 Void Migration

To begin, we analyze the void migration rate for a single void by tracking the center, leading and trailing edge velocities, which are plotted in Fig.4.12. Edges are identified by tracking the greatest and least value of the $\rho = 0.5$ contour along the midpoint of the y-axis. Tracking along the midpoint provides information on the concave deformation of the void that can be visualized in Fig. 4.13. From Fig. 4.12, we see initialization of void movement and a steady slowing of void migration with the leading edge decelerating more quickly.

48

Initially however, the leading edge is quicker to accelerate resulting in a pointed leading edge as seen in Fig. 4.13 (a) before the concave deformation begins.
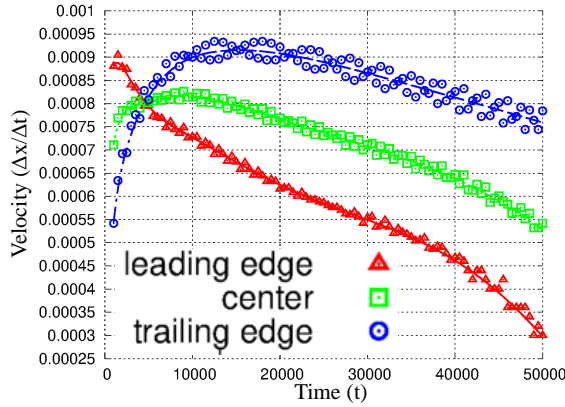
Figure 4.12: Plotted are the velocities of a single void migrating from a simulation with atomic mobility of 1.0, $\varepsilon_{ik}^* = 0.0$, and $\Delta\phi = 2.0$.

Here, we analyze the chemical potential and relative displacement along the axis of electron current to demonstrate the mechanisms of this deformation and migration in a void migration simulation with an eigenstrain of $\varepsilon_{ik}^* = -2.5\%$ and $\Delta\phi = 2.0$. To help, we have plotted the chemical potential field along a $\rho = 0.5$ contour of the vacancy density field with black arrows demonstrating diffusion direction and scale in Fig. 4.13 for times of 10000, 40000, and 60000. Initially and seen in Fig. 4.13 (a), we display an increased chemical potential along the backside of the void that retains its shape throughout the voids migration. Alternatively and also visualized in (a) is the decreased chemical potential along the leading and side edges of the void. A decreased chemical potential drives vacancy density to these locations resulting in the more pointed leading edge initially, and ultimately, the shape distortions seen in the (b and c). In Fig. 4.13 (b), the sides of the void have begun to overtake the leading edge of the void resulting in a concave void shape similar to experimental results from Branch et. al.[39]. We propose that this deformation occurs as the unimpeded electron wind along the sides of the void result in a larger amount of

49

electromigration than the center of the void where electromigration is limited to only the forces of the electron current wrapping around the void. This effect is more completely visualized by the diffusion directions plotted in Fig. 4.13 (c). Here, predominant diffusion of vacancy density is along the two protruding edges and backside of the void. We also investigated the effects of electromigration-mediated void migration on relative displacement in the direction of electron current as plotted in Fig. 4.14. In this figure, we present the relative displacement field in the z-axis of the compressed interconnect with a black contour outlining the void edge ($\rho = 0.5$) at times of 10000, 40000, and 60000. Relative displacement
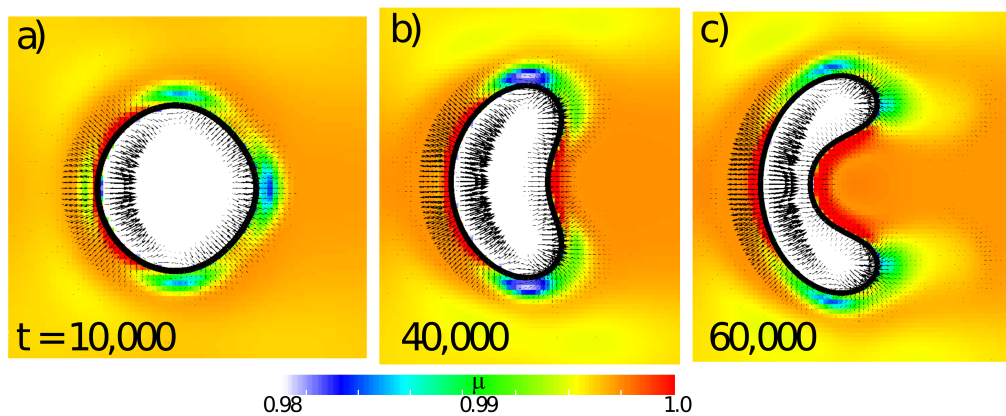
Figure 4.13: Displayed here is migration of a single void (Black contour, $\rho = 0.5$) at times of 10000 (a), 40000 (b), and 60000 (c) plotted over the chemical potential field. Black arrows represent the direction and scale of vacancy density diffusion. The simulation had an atomic mobility of 1.0, $\varepsilon_{ik}^* = -2.5\%$, and $\Delta\phi = 2.0$.

was used in this plot to demonstrate the state of the interconnect at each time step and not compare across time steps. In (a) of Fig. 4.14, we see compression along the leading and trailing edges of the void indicative of a migrating void. Along the side edges of the void though, we see significant tension in the z-direction, which we associate with larger electromigration forces. In Fig. 4.14(b) and as the void begins to concavely deform, we
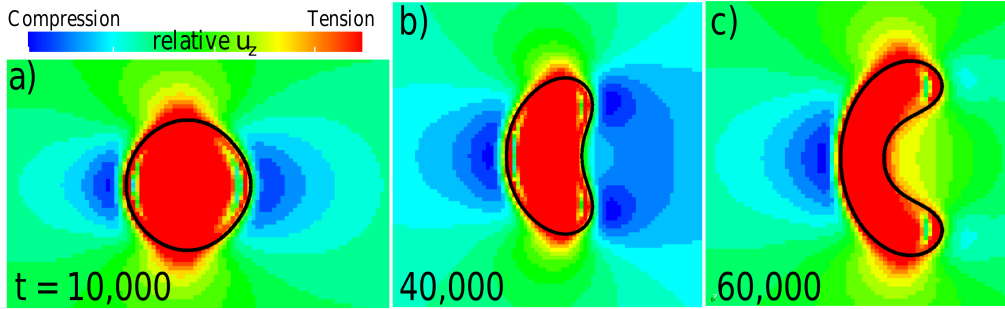
Figure 4.14: Displayed here is migration of a single void (Black contour, $\rho = 0.5$) at times of 10000 (a), 40000 (b), and 60000 (c) plotted over a relative displacement of z field. Simulation had an atomic mobility of 1.0, $\varepsilon_{ik}^* = -2.5\%$, and $\Delta\phi = 2.0$.

see a similar phenomenon to (a) but with relative compression at the pair of leading edges. Ultimately and seen in (c), the deformation of the void builds tension around the center and concave portion of the void. These compressive forces slightly slow the migration of he void as discussed below but are largely overpowered by electromigration; therefore, the migrating void's morphological evolution is similar.
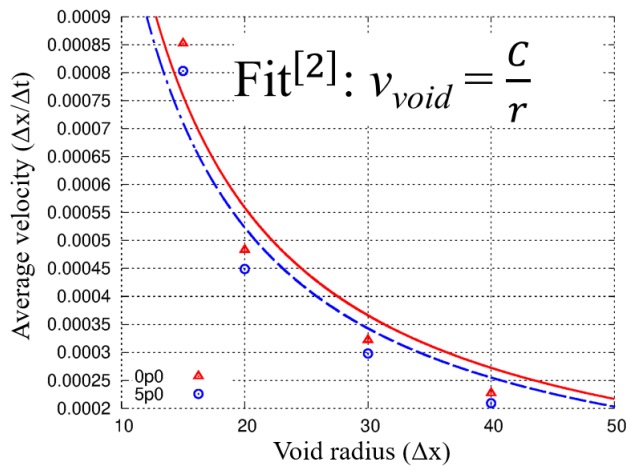
Figure 4.15: Plotted above are average rates of void migration by void size fitted to a $1/r$ relationship as proposed in Artz's work[2]. Void size is determined by initial radius and sizes simulated have radii of 15, 20, 30, and 40.

Void migration velocity is dependent on void radii and interconnect width as discussed by Artz and coworkers[2]. They propose that the migration of larger voids requires more mass transport and therefore more time; however, they add that migration velocity can significantly increase with a large enough ratio of void size to interconnect width due to increase current density from void confinement. Ignoring effects from interconnect confinement they propose the following relationship that follows a $1/r$ relationship with r representing void radius:

$$v_{void} = 2\frac{\delta}{r}\frac{D_s Z^* e\rho j}{kT},$$

(4.2)

where δ is the interface width, r is the void radius, D_s is the diffusion coefficient associated with the void surface, T is temperature, j is current density, D_o is the diffusion coefficient, Z^* is effective charge, e is electron charge, and ρ is the resistivity of the interconnect.

In our work, we have fitted the above relationship to our void migration data at eigenstrains of 0 and -5% in Fig. 4.15. From this plot we can make three conclusions: model 1 and model 2 both result in expected trends for the relationship between void radius and velocity of migration (validating model 2 with theory and model 1, Fig. 4.2), compression has little effect on the $1/r$ correlation between void migration rate and void size, and that compression in an interconnect slows average void velocity at a decreasing effect with void size. This decreasing effect of compression with void size is attributed to the the slower deformation to concavity, which effects void migration rate as seen in Fig. 4.12 and 4.16 (a). In Fig. 4.12 there is substantial variation in the void velocity of leading and trailing edges with a more significant decrease in void velocity of the leading edge, which indicates the increased concavity of the void. However and in Fig. 4.16 (a), we display the comparison between the trailing edges at void's with radii of 15, 20, and 30 Δx. Here we can visualize the slower velocities as well as slower rates of deformation indicated by the
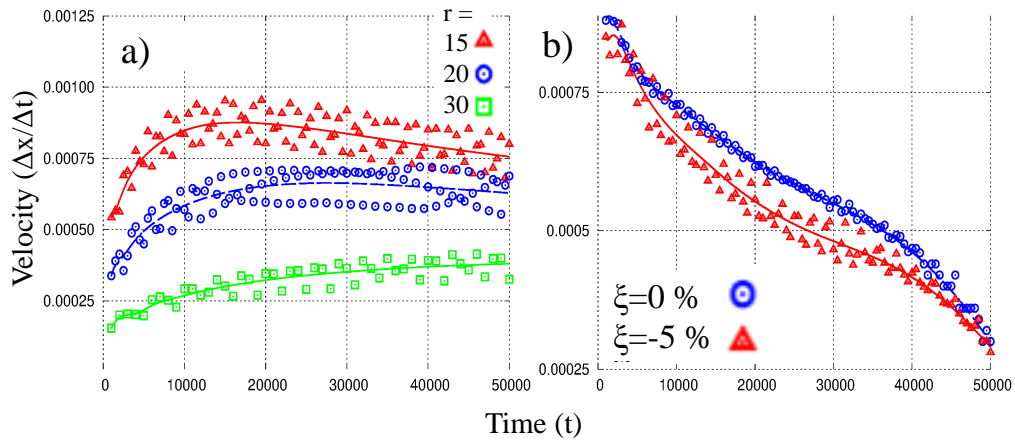
Figure 4.16: In (a) we display the variations in void migration rates for the trailing edges of voids with sizes of 15, 20, and 30, and in (b) we display the void velocity difference of a void's leading edge with and without a compressive force ($\varepsilon_{ik}^* = 0, \, -5\%$)

different shapes of each curve with increasing void radius. In Fig. 4.16 (b) we plot the effects of eigenstrain on the velocity of the leading edge of a void with a radius of 15 Δx. Initially, we see an increase of the void deformation indicated by the the slower velocity of the leading edge; however, once deformation becomes significant at approximately 30000 time steps the leading edge velocity in both simulations become similar. We propose this is due to the increased chemical potential as concavity increases, which diminishes the relative contribution from the interconnect's eigenstrain.

4.2.2 Void Coalescence and Budding

In this section, we analyze the diffusional mechanisms of void budding and coalescence as well as the role of interfacial energy effects on void deformation. First we analyze the coalescence of a pair of voids with radii of 20 Δx as seen in Fig. 4.17. Plotted in this figure are the chemical potential fields for the void pair at times of 1000 (a), 6000 (b), and 30000

(c) with a black contour at $\rho = 0.5$ and black arrows representing the vacancy diffusion directions and scale. The simulation presented had no compression effects ($\varepsilon_{ik}^* = 0\%$) and no forces from electromigration ($\Delta\phi = 0$) to solely view coalescence of the void pair. As seen in these simulation images, the predominate areas of vacancy diffusion are around the neck of the void pair resulting in symmetric coalescence of the voids. The distribution of chemical potential around the void pair is uniform primarily due to the consumption of nearby vacancies by the joining voids. As the void pairs resolve the curvature of the necking region, as seen in Fig, 4.17 (c), vacancy diffusion is also seen in significant amounts on the outer edges of the void pair, indicating further coalescence to a single circular void in time.

Comparing the results of coalescence simulations with no electromigration or compression effects with Fig. 4.18, we can determine the role of compression and electromigration effects on coalescence and resultant budding of new voids. Here in Fig. 4.18, we examine the chemical potential field of a pair of identical voids (radii = 20 and contour of $\rho = 0.5$ in black) migrating under an electric field strength of 3.0, compressive eigenstrain of $\varepsilon_{ik}^* = -2.5\%$, and with diffusion directions and scale depicted by black arrows at times of 6000, 30000, and 50000 time steps. In (a) coalescence of the void pair has begun due to the severe angles of the overlapping circles in the initial condition. However, also in (a) we

view the lack of significant diffusion around the necking area with the majority of diffusion taking place along the back and front sides of the void pair. The chemical potential along the back and front sides of the void pair are asymmetric. A regular band of chemical potential minima can be found along the entire trailing edge of the void pair and a wake of chemical potential minima is found along the perimeter of the void pair reaching forward. Both of these trends exacerbate as the simulation continues as seen in Fig. 4.18 (b). Also, these regions of higher chemical potential along the surface of the void pair near the necking site have little to no vacancy diffusion. As the leading void continues to elongate, the neck length decreases until budding of the void pair is seen in Fig. 4.18 (c). The chemical

Figure 4.17: Displayed here is coalescence of a pair of voids (Black contour, $\rho = 0.5$) at times of 1000 (a), 6000 (b), and 30000 (c) plotted over the chemical potential field. Black arrows represent the direction and scale of vacancy density diffusion. The simulation had an atomic mobility of 1.0, $\varepsilon_{ik}^* = 0\%$, and $\delta\phi = 0.0$.

Figure 4.18: Displayed here is coalescence and budding of a pair of voids (Black contour, $\rho = 0.5$) at times of 6000 (a), 30000 (b), and 50000 (c) plotted over the chemical potential field. Black arrows represent the direction and scale of vacancy density diffusion. The simulation had an atomic mobility of 1.0, $\varepsilon_{ik}^* = -2.5\%$, and $\delta\phi = 3.0$.
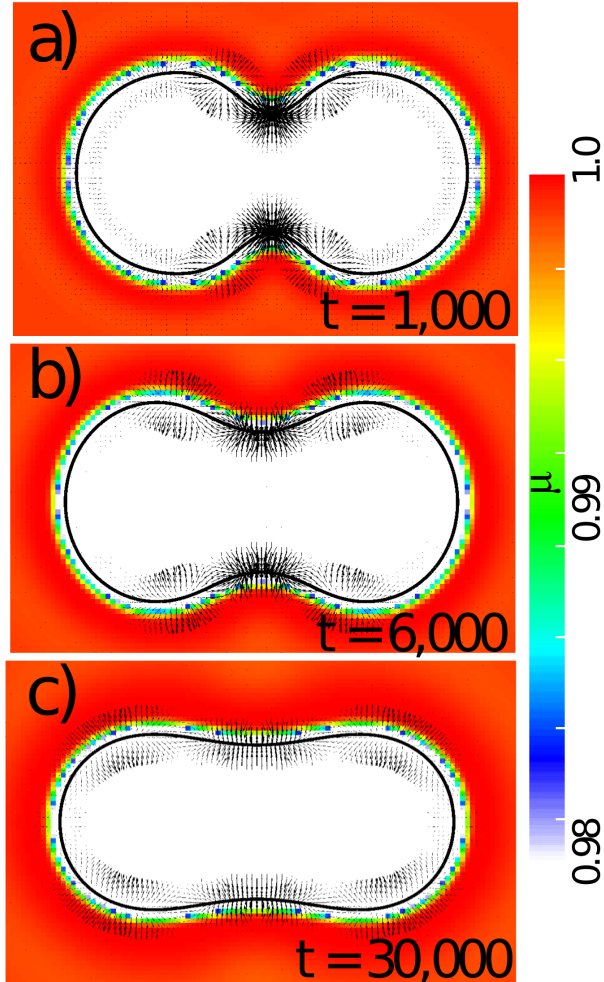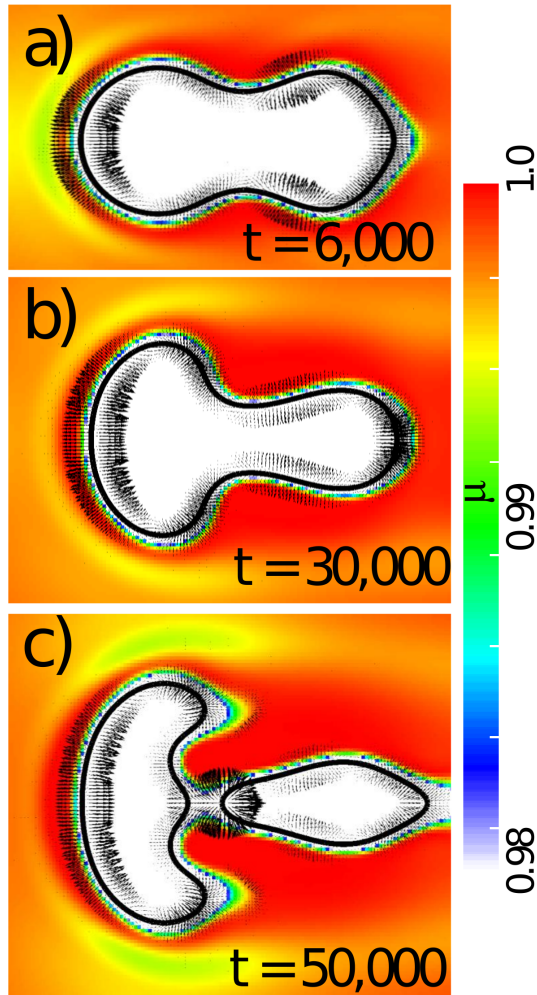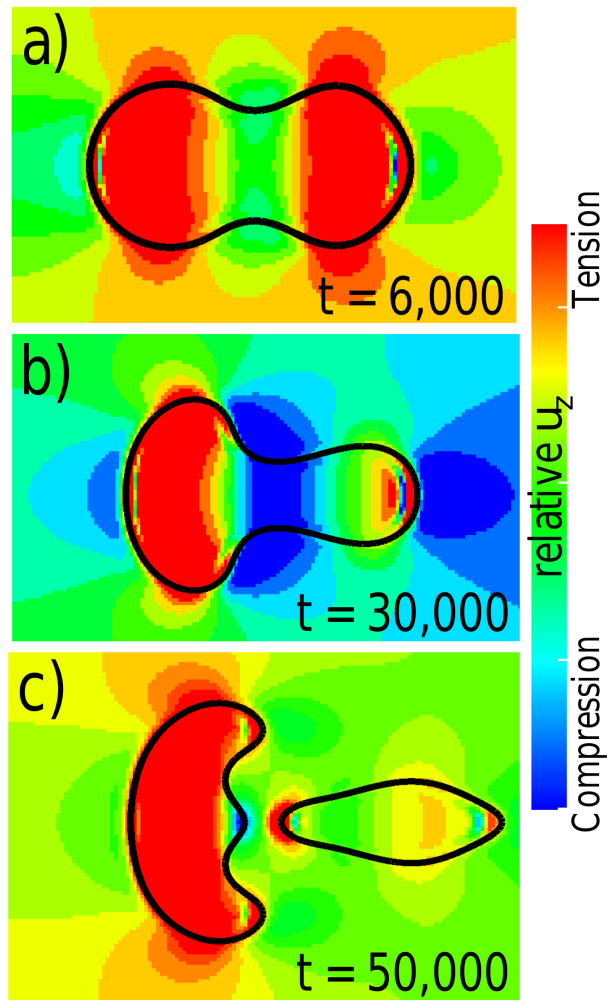
Figure 4.19: Displayed here is coalescence and budding of a pair of voids (Black contour, $\rho = 0.5$) at times of 6000 (a), 30000 (b), and 50000 (c) plotted over a relative displacement of z field. The simulation had an atomic mobility of 1.0, $\varepsilon^*_{ik} = -2.5\%$, and $\delta\phi = 3.0$.

potential wake is formed from vacancy density increasing as it flows around the trailing edge of the void from cathode to anode. Chemical potential is at its lowest in the interconnect around the top and bottom edges of the trailing void, which increases the growth of the void into those directions. This effect can be immediately compared with the leading void in the void pair that lacks this chemical potential sink and therefore does not grow similarly. Next, we investigate the behavior of mechanical stresses throughout void coalescence and budding. In Fig. 4.19 we plot the relative displacement in the direction of current flow for the same simulation presented above in Fig. 4.18. Relative displacement was again used to demonstrate comparisons at each time step and not across multiple time steps. As seen in Fig. 4.19 (a) we have small amounts of relative compression at the trailing edge of the void pair with large amounts of tension across the bottom and top edges of the void pair. As the leading void begins to elongate and reduce the neck size of the void pair as seen in Fig. 4.19 (b), the relative tension on the top and bottom edges of the leading void reduce significantly while this tension is maintained on the top and bottom edges of the trailing void. Further and in (c), the relative tension is maintained along the top and bottom edges of the trailing void upon the budding of a new void. There is some tension along the trailing and leading edges of the newly budded void.

In Fig. 4.20, we compare the neck length over time for simulations with and without an eigenstrain of -2.5% at two different κ values (0.33 and 3.0), a parameter directly proportional to interfacial energy, to examine the relationship of eigenstrain, interfacial energy, and void morphology through coalescence. All simulations had a $\Delta\phi = 0.5$ to avoid severe budding which could shroud our intended examination. The first relationship we examine in (a) is that as interfacial energy is increased eigenstrain has significantly less effect on the behavior of the void pair. In the simulation with increased interfacial energies ($\kappa = 3.0$) there is very little difference in the evolution of the void pair through coalescence with the only exception being a slight elongation of the void's leading edge relative to the simula-
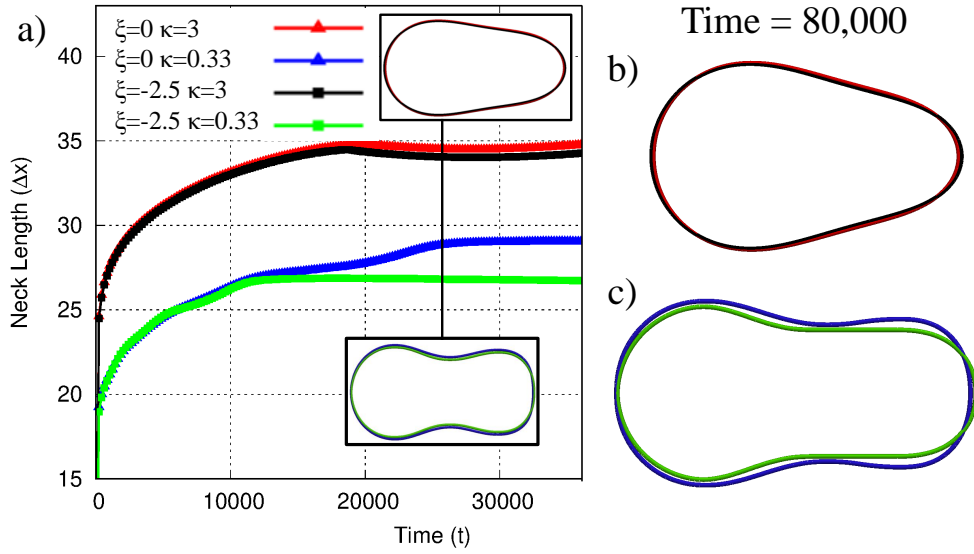
Figure 4.20: In (a) we plot the neck length of four simulations where $\kappa = 0.33, 3.0$ and $\varepsilon_{ik}^* = 0, -2.5\%$ to examine the relationship between interfacial energy and eigenstrain. Simulations were ran with a $\Delta\phi = 0.5$. Inset are contours of $\rho = 0.5$ for the corresponding simulations at a time of 26000. In (b) and (c) we have larger contour maps of the simulations at a time of 80000 to demonstrate the differences between the four simulations.

tion without eigenstrain. This can be seen more clearly in Fig. 4.20 (b). Another point to note is the significantly quicker resolution of the void pair with higher interfacial energy, but this result is expected. However and for the simulations with a smaller interfacial energy ($\kappa = 0.33$), the differences between simulations with and without eigenstrain are more noticed, and coalescence results in a different shape for the void pair as made apparent by the smaller equilibrium neck length in Fig. 4.20 (a). Here, the interfacial energy lacked the strength to fully coalesce the void pair, and the eigenstrain compressed the leading void into a more elongated shape as seen in (c). This demonstrates a force balance between the interfacial energy, eigenstrain, and forces of electromigration that requires further study to fully encapsulate and understand. However, we can conclude that coalescence is quicker and small eigenstrains become negligent forces at higher interfacial energies.

59

Chapter 5

CONCLUSIONS

We have simulated electromigration-mediated defect evolution in poly- and monocrys-talline interconnects utilizing a phase-field model in both 2- and 3-dimensions. In this work, we studied the effect of local atomic mobility environments, the effect of increased current density, and microstructure effects. Specifically, we found the relationships of grain boundary misalignment with respect to applied electric field and slit formation velocity, as well as developed a mechanistic explanation for our results. Further relationships were gathered between grain size of equiaxed microstructure and defect evolution rate, and we probed the need for 3-D considerations in the model as well as 4-D characterization techniques. Also determined from this work were insights into void coalescence, migration, and budding and the effect of electromigration, eigenstrain, and vacancy diffusion on these phenomenon. Below the main conclusions from this work are summarized:

1. In a network of equiaxed grains, the grain size, as expected, follows an inverse pro-portionality with the slit propagation rate. GB alignment has a significant influence on the defect kinetics; when the GB is perfectly aligned along the direction of cur-rent flow, the gradient vectors wrap around the slit tip resulting in a mass transport flux directing down the GB. However, increasing the magnitude of GB misalignment w.r.t. externally applied electric field results in more electromigration into the bulk, rather than along the GB, thereby, retarding the slit propagation velocity.

2. When the mobility ratio, M_{GB}/M_s, is less than 100, mixed mode, which imbibes the characteristics of both surface drift as well as slit growth, occurs, significantly lower-ing the defect propagation rates. This is primarily caused by the mass transport along

the surface of the interconnect which replenishes the groove root. Curving of inter-connect surface occurs when the M_{GB}/M_s ratios are small, which further increases the replenishment of the groove root.

3. Phase-field simulations of defects evolution in a network of randomly-distributed grains reveal that GBs that are equally misaligned with respect to the external electric field result in identical slit propagation rate, while a severe misalignment can halt the defect progression, altogether. While this finding is corroborated through our 3-D simulations, the slit formation propagation is found to be several times faster when compared with 2-D simulations. This increase in defect evolution velocity is due to the availability of numerous diffusional pathways in 3-D as opposed to 2-D where the defect is constrained to propagate along a line. Such a difference in growth kinetics emphasizes the need for 4D characterization of EM-mediated defects for their efficient mitigation.

4. Electromigration reduces the chemical potential around the void edges during migra-tion resulting in the deformation of the void. This effect is slowed down by compres-sive stresses, but does not prevent the deformation. The void migration rate decreases with deformation.

5. A void pair coalescing or budding new voids relies on the balance of factors: inter-facial energy of the void pair, electromigration strength, and compressive stresses. Ultimately, increasing interfacial energy will increase the likelihood of void coales-cence, while increases electromigration strength will result in budding of new voids. Compressive forces slow each process, but are small in comparison to electromigra-tion and interfacial energy.

REFERENCES

[1] Shivani Vemulapalli. *Phase-Field Modeling of Electromigration-Mediated Morphological Evolution of Voids in Interconnects*. 2020.

[2] W. D. Nix and E. Arzt. On Void Nucleation and Growth in Metal Interconnect Lines under Electromigration Conditions. *Mettalurgic Transactions A*, 23A:2007–2013, 1992.

[3] H. Ceric and S. Selberherr. Electromigration in submicron interconnect features of integrated circuits. *Mater. Sci. Eng. Rep.*, 71(5-6):53–86, 2011.

[4] P. S. Ho and T. Kwok. Electromigration in metals. *Rep. Prog. Phys.*, 52(3):301–348, mar 1989.

[5] A. Mukherjee, K. Ankit, R. Mukherjee, and B. Nestler. Phase-field modeling of grain-boundary grooving under electromigration. *J. Electron. Mater.*, 45:6233–6246, Dec 2016.

[6] A. Mukherjee, K. Ankit, M. Selzer, and B. Nestler. Electromigration-induced surface drift and slit propagation in polycrystalline interconnects: Insights from phase-field simulations. *Phys. Rev. Appl.*, 9:044004, Apr 2018.

[7] ITRS. International Technology Roadmap for Semiconductors. Technical report, 2011.

[8] T. O. Ogurtani and O. Akyildiz. Grain boundary grooving and cathode voiding in bamboo-like metallic interconnects by surface drift diffusion under the capillary and electromigration forces. *J. Appl. Phys.*, 97(9):093520, may 2005.

[9] O. Akyildiz and T.O. Ogurtani. Grain boundary grooving induced by the anisotropic surface drift diffusion driven by the capillary and electromigration forces: Simulations. *J. Appl. Phys.*, 110(4):043521, aug 2011.

[10] T. O. Ogurtani and E. E. Oren. Electromigration-induced void grain-boundary interactions: The mean time to failure for copper interconnects with bamboo and near-bamboo structures. *J. Appl. Phys.*, 96(12):7246–7253, dec 2004.

[11] W. Li, C. M. Tan, and Y. Hou. Dynamic simulation of electromigration in polycrystalline interconnect thin film using combined Monte Carlo algorithm and finite element modeling. *J. Appl. Phys.*, 101(10):104314, may 2007.

[12] C. Basaran and M. Lin. Damage mechanics of electromigration in microelectronics copper interconnects. *Int. J. Materials and Structural Integrity*, 1(4):016039, 2007.

[13] K. Croes, Y. Li, M. Lofrano, C. J. Wilson, and Z. Tokei. Intrinsic study of current crowding and current density gradient effects on electromigration in BEOL copper interconnects. In *2013 IEEE International Reliability Physics Symposium (IRPS)*, pages 2C.3.1–2C.3.4. IEEE, apr 2013.

[14] F. He and C. M. Tan. 3D Simulation-Based Research on the Effect of Interconnect Structures on Circuit Reliablity. *World Journal of Modeling and Simulation*, 8:271284, July 2012.

[15] S. Chakraborty, P. Kumar, and A. Choudhury. Phase-field modeling of grain-boundary grooving and migration under electric current and thermal gradient. *Acta Mater*, 153:377–390, jul 2018.

[16] C. K. Hu, R. Rosenberg, and K. Y. Lee. Electromigration path in cu thin-film lines. *Appl. Phys. Lett.*, 74(20):2945–2947, 1999.

[17] D. A. Porter, K. E. Easterling, and M. Youssef Abdelraouf Sherif. *Phase Transformations in Metals and Alloys*. CRC Press, Feb 2009.

[18] E. Baibuz, S. Vigonski, J. Lahtinen, J. Zhao, V. Jansson, V. Zadin, and F. Djurabekova. Migration barriers for surface diffusion on a rigid lattice: Challenges and solutions. *Comp. Mater. Sci.*, 146:287 – 302, 2018.

[19] D. Contestable-Gilkes, D. Ramappa, M. Oh, and S. M. Merchant. Effect of copper seed aging on electroplating-induced defects in copper interconnects. *J. Electron. Mater.*, 31:1047–1051, Oct 2002.

[20] E. Glickman and M. Nathan. On the unusual electromigration behavior of copper interconnects. *J. Appl. Phys.*, 80(7):3782–3791, 1996.

[21] M. S. Park and R. Arróyave. Early stages of intermetallic compound formation and growth during lead-free soldering. *Acta Mater.*, 58(14):4900–4910, 2010.

[22] M. S. Park, S. L. Gibbons, and R. Arróyave. Phase-field simulations of intermetallic compound evolution in cu/sn solder joints under electromigration. *Acta Mater.*, 61(19):7142–7154, 2013.

[23] M. Mahadevan and R. Bradley. Simulations and theory of electromigration-induced slit formation in unpassivated single-crystal metal lines. *Phys. Rev. B*, 59(16):11037–11046, 1999.

[24] J. Santoki, A. Mukherjee, D. Schneider, M. Selzer, and B. Nestler. Phase-Field Study of Electromigration-Induced Shape Evolution of a Transgranular Finger-Like Slit. *J. Electron. Mater.*, 48(1):182–193, 2019.

[25] L. Klinger and L. Levin. Interface instability in an electric field. *J. Appl. Phys.*, 78(3):1669–1672, 1995.

[26] A. F. Bower and S. Shankar. A finite element model of electromigration induced void nucleation, growth and evolution in interconnects. *Mod. Sim. Mater. Sci. Eng.*, 15(8):923–940, 2007.

[27] Y.-W. Chang, Y. Cheng, L. Helfen, F. Xu, T. Tian, M. Scheel, M. Di Michiel, C. Chen, K.-N. Tu, and T. Baumbach. Electromigration mechanism of failure in flip-chip solder joints based on discrete void formation. *Scientific Reports*, 7(1):1–16, 2017.

[28] C. L. Gan and M. K. Lim. 5 - voiding in copper interconnects during electromigration. In Choong-Un Kim, editor, *Electromigration in Thin Films and Electronic Devices*, Woodhead Publishing Series in Electronic and Optical Materials, pages 113 – 134. Woodhead Publishing, 2011.

[29] R. L. [de Orio], H. Ceric, and S. Selberherr. A compact model for early electromigration failures of copper dual-damascene interconnects. *Microelectronics Reliability*, 51(9):1573 – 1577, 2011. Proceedings of the 22th European Symposium on the Reliability of electron devices, failure physics and analysis.

[30] H. Mario, M. K. Lim, and C. L. Gan. Impact of pre-existing voids on electromigration in copper interconnects. In *2012 19th IEEE International Symposium on the Physical and Failure Analysis of Integrated Circuits*, pages 1–5. IEEE, 2012.

[31] Z. Tang and F. G. Shi. Effects of preexisting voids on electromigration failure of flip chip solder bumps. *Microelectronics Journal*, 32(7):605–613, 2001.

[32] S. B. Liang, C. B. Ke, W. J. Ma, M. B. Zhou, and X. P. Zhang. Numerical simulations of migration and coalescence behavior of microvoids driven by diffusion and electric field in solder interconnects. *Microelectronics Reliability*, 71:71–81, 2017.

[33] Z. Suo. *Reliability of interconnect structures. pp. 265-324 in Volume 8: Interfacial and Nanoscale Failure*. Elsevier, Amsterdam, 2003.

[34] J. W. Cahn and J. E. Hilliard. Free energy of a nonuniform system. i. interfacial free energy. *J. Chem. Phys.*, 28(2):258–267, 1958.

[35] J. W. Cahn. On spinodal decomposition. *Acta Metall. Mater.*, 9(9):795 – 801, 1961.

[36] S. M. Allen and J. W. Cahn. A microscopic theory for antiphase boundary motion and its application to antiphase domain coarsening. *Acta Metall. Mater.*, 27(6):1085 – 1095, 1979.

[37] M. Fleck, L. Mushongera, and D. et al. Pilipenko. On phase-field modeling with a highly anisotropic interfacial energy. *Eur. Phys. J. Plus*, 126, 2011.

[38] M.E. Glickman. *Diffusion in Solids: Field Theory, Solid-State Principles, and Applications*. Wiley, New York, 1999.

[39] M. B. Kelly, S. Niverty, and N. Chawla. Four dimensional (4d) microstructural evolution of cu6sn5 intermetallic and voids under electromigration in bi-crystal pure sn solder joints. *Acta Mat.*, 189:118–128, 2020.